Alma Mater Studiorum - Università di Bologna

_____

SCUOLA DI SCIENZE

Dipartimento di Chimica Industriale "Toso Montanari"

Corso di Laurea Magistrale in

Chimica Industriale

Classe LM-71 - Scienze e Tecnologie della Chimica Industriale

Computational characterization of carbazole-benzonitrile derivatives for applications in Organic Light Emitting Diodes

Tesi di laurea sperimentale

CANDIDATO

Francesco Rizzo

RELATORE

Prof. Luca Muccioli

CORRELATORE

Prof. Silvia Orlandi

Prof. Alberto Arcioni

_____

Anno Accademico 2019-2020
_____

Contents

ABSTRACT:

The technology of Organic Light-Emitting Diodes (OLED) has now reached such a high level of reliability that it can be used in various applications already on the marked. The required light emission efficiency can be achieved by transforming the triplet excitons into singlet states through Reverse InterSystem Crossing (RISC), which is the main process of a general mechanism called thermally activated delayed fluorescence (TADF).

In this thesis, we theoretically analyzed two carbazole-benzonitrile (donor-acceptor) derivatives, 2,5-di(9*H*-carbazol-9-yl)benzonitrile (p-2CzBN) and 2,3,4,5,6-penta(9*H*-carbazol-9-yl)benzonitrile (5CzBN), and addressed the problem of how donor-acceptor (D-A) or donor-acceptor-donor (D-A-D) flexible molecular architectures influence the nature of the excited states and the emission intensity. Furthermore, we analyzed the RISC rates as a function of the conformation of the carbazole lateral groups, considering the first few electronic states, S_0, S_1, T_1 and T_2, involved in the TADF process. The two prototype molecules, p-2CzBN and 5CzBN, have a similar energy gap between the first singlet and triplet states (ΔE^{ST}, a key parameter in the RISC rate), but different TADF performances. Therefore, other parameters must be considered to explain their different behavior.

The oscillator strength of p-2CzBN, never tested as emitter in OLEDs, is similar to that of 5CzBN, which is an active TADF molecule. We also note that the presence of a second T_2 triplet state, lower in energy than S_1 only in 5CzBN, and the reorganization energies, associated with RISC processes involving T_1 and T_2, are both important factors in differentiating the rates in p-2CzBN and 5CzBN. For p-2CzBN, the RISC rate from T_2 to S_1 is surprisingly higher than that from T_1 to S_1, in disagreement with El-Sayed rules, due to a large reorganization energy associated to the T_1 to S_1, process; while the contrary occurs for 5CzBN. These insights are important for understanding the photophysics of the TADF process, underlining a possible important role of higher triplet states, and for designing new TADF emitters based on the benzo-carbazole architecture.

Chapter 1

Introduction

Figure 1.1 Examples of present organic semiconductor applications OLEDs in Samsung and Philips flexible display.

The technology of organic light-emitting diodes (OLED) has now reached common use in various commercial devices, such as lighting panels and displays for smartphones (figure 1.1)[1], tablets, laptops and TVs. The world's first efficient OLED, consisting of a double layer structure of organic thin films, was developed by Ching W. Tang and Steven Van Slyke in 1987[2]. Today OLEDs are constituted of many superimposed organic layers, vapor-deposited between anode and cathode, such as shown in figure 1.2. In all types of devices, the hole / electron injection layers (HIL/EIL) are used for charge injection in hole/electron transport layers (HTL/ETL) and an emission (EML) is used for light emission[3]. There, electrons and holes coming from the electrodes via the transport layers recombine in single (emitter) molecule, forming a bound electron pair, called exciton by physicists, and excited state in a more chemical language that implies its complete localization in a single molecular unit.
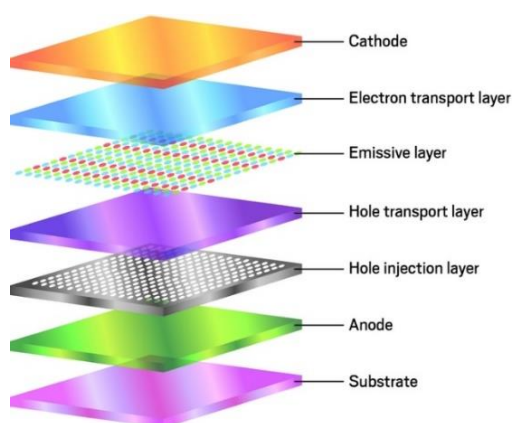
Figure 1.2 Multi-layer structure employed in current OLED products.

There are in principle multiple physical processes exploitable for generating light from these excitons. All must face the problem that, due to electron spin statistics upon hole and electron recombination, only 25% of the excitons generated by the current are singlet states, for which the selection rules for electronic transitions allow the emissive decay to the (singlet) ground state. If only

this mechanism, known as prompt fluorescence (PF), is available, it sets the theoretical limit of Internal Quantum Efficiency (IQE, the ratio between the number of emitted photons and the number of injected charges) to 25 %. The 75 % of triplet excitons are generally non-emissive due to the spin forbidden transition from T_1 to S_0[4]. Spin-flip from pure S_1 to pure T_1 states through intersystem crossing (ISC) is also forbidden, due to their difference in spin multiplicities, but it becomes possible when their wave functions are mixed through spin-orbit coupling (SOC)[5,6]. By including a heavy metal such as Iridium or Platinum in an organic molecule, SOC is enhanced and a strong mixing of spin orbitals in S and T states occurs, resulting in an efficient $S_1 \rightarrow T_1$ conversion and in the ensuing phosphorescence process (from T_1 to S_0 states) with almost 100 % of IQE. Recent metal-based OLED emitters based on phosphorescent metallo-organic molecules can reach External Quantum Efficiency (EQE, the ratio between the number of photons actually exiting the device and the number of injected charges) close to 30 %[7]. However, the stability of metal-based OLEDs in the blue emission region has yet to be improved[8]. Furthermore, the drawback of using rare metal-based materials is that they are expensive and toxic.

Recently, a new design strategy has been adopted that exploits fully organic emitters through a phenomenon known as Thermally Activated Delayed Fluorescence (TADF). The concept of TADF is not new as it was first rationalized into solid uranyl salts by Perrin in 1929[9]. TADF is based on a thermally activated reverse (up-conversion) intersystem crossing (RISC) from the lowest triplet excited state T_1 to the lowest singlet excited state S_1, leading to a delayed Fluorescence (DF) (figure 1.3, third diagram). As a result, the IQE can easily reach up to 100 %. However, TADF based OLEDs still give poor performances in the red and blue regions, and also have a too broad emission spectrum[10,11] while to achieve high color purity in display applications, narrow emission is required[12]. To achieve high efficiency, TADF emitters should have a fast radiative decay, but also a small energy gap between S_1 and T_1 to promote the RISC process. A small ΔE^{ST} can be achieved by intramolecular CT excitations from the ground state, a strategy that, in practice, minimizes the exchange energy of excited state S_1 and brings its energy closer to that of the triplet state T_1. To obtain a CT character, the wavefunctions of S_0 and S_1 (and T_1) must be, as far as possible, localized in different regions of the molecule, but unfortunately this also minimizes the S_0-S_1 transition dipole and oscillator strength, and in practice leads to molecules with small radiative rates. In this regard, Monkman and collaborators have suggested a key role of the presence of a locally excited (LE) triplet state in near resonance with CT states, which could lead to an improvement of the interconversion mechanism[13]. To date, a full understanding of photophysics of the TADF mechanism is still under discussion and must be achieved to optimize the performance of materials and devices.
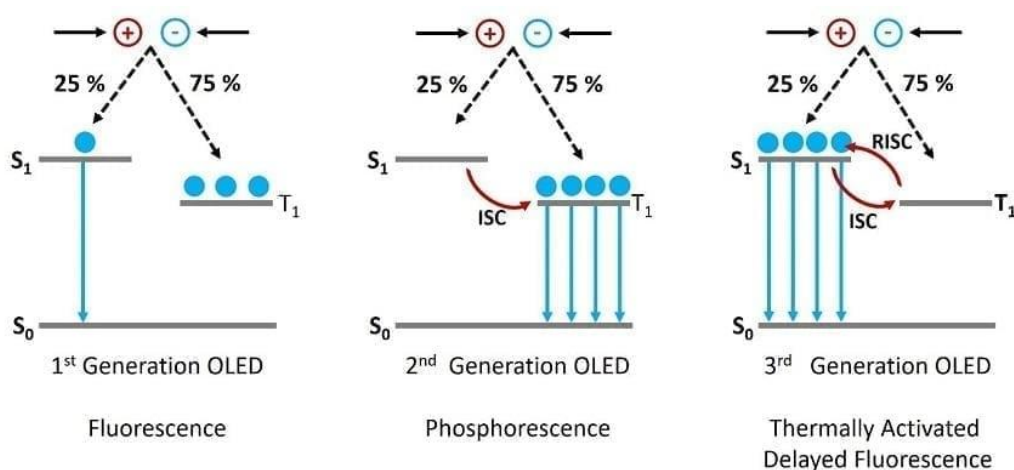
Figure 1.3 The evolution of the strategies for obtaining light emission in Organic Light-Emitting Diodes (OLEDs).

The design strategy to harvest the non-radiative triplet excitons via RISC, in a one-electron's frozen-core approximation, is to minimize the spatial overlap between the Highest Occupied Molecular Orbital (HOMO, representing the ground state wavefunction) and Lowest Unoccupied Molecular Orbital (LUMO, representing S_1 and T_1 wavefunctions), since it leads to singlet and triplet first excited states close in energy. The most common molecular design of TADF emitter therefore consists of covalently linked donor and acceptor that efficiently confine hole and electron densities over different spatial regions[14]. The formation of excited states with strong CT character effectively leads to a reduced overlap between the HOMO and LUMO, resulting in a small ΔE^{ST}[15]. However, the presence of groups of donors and acceptors is not a sufficient condition to minimize ΔE^{ST}, but an almost orthogonal geometry between those functional groups is also necessary to avoid extended conjugation[16]. Therefore, the dihedral angles between the donor (D) and acceptor (A) fractions also play an important role in the TADF emitters, and can vary significantly between the regioisomers of the same emitter. Furthermore, the small ΔE^{ST} is not the only parameter to determine an efficient RISC. It is worth emphasizing once again that recent literature also addresses the presence of the spin-vibronic coupling and the mixing of charge transfer and localized excitation states to be useful for the RISC[17].

In this thesis project, we theoretically investigate two selected carbazole benzonitrile derivatives, which are 2,5-di (9H-carbazol-9-yl) benzonitrile (p-2CzBN) and 2,3,4,5,6-penta (9H-carbazol-9-yl) benzonitrile (5CzBN). The properties of p-2CzBN and 5CzBN are compared with those of 2CzBN and 4CzBN (previously studied also in a similar work) and with the properties of 5CzBN synthesized by Adachi and co-workers18. Carbazole plays the role of the electron donor group while benzonitrile acts like the group that accepts electrons. From the experimental results, 5CzBN as well as 4CzBN are active TADF emitters; while 2,3 2CzBN is TADF inactive and p-

5

2CzBN was never tested. Therefore, p-2CzBN and 5CzBN are theoretically studied and the TADF mechanism sectioned by means of DFT and TDA-DFT calculations. We will address the problem of how flexible donor-acceptor or donor-acceptor-donor molecular architectures influence the nature of the excited states and RISC rates, which play a key role in the TADF process. According to Adachi and co-workers[18], in fact, only D-A-D type molecules are TADF active. For this reason, we decided to study both the 5CzBN and the p-2CzBN molecules, which share this structural architecture.

This thesis is organized as follows: Chapter 2 provides a more detailed description of TADF-based OLEDs and the challenge of designing TADF chromophores. The analysis of the electronic structure of p-2CzBN and 5CzBN is reported in Chapter 3. In Chapter 4, we characterize the nature of the excited states and their interconversion rates. The conclusions are drawn in Chapter 5.

Chapter 2

Background

This chapter provides a photophysical background of the main electronic processes that regulate thermally activated delayed fluorescence, with particular attention to its application on organic light emitting diodes.

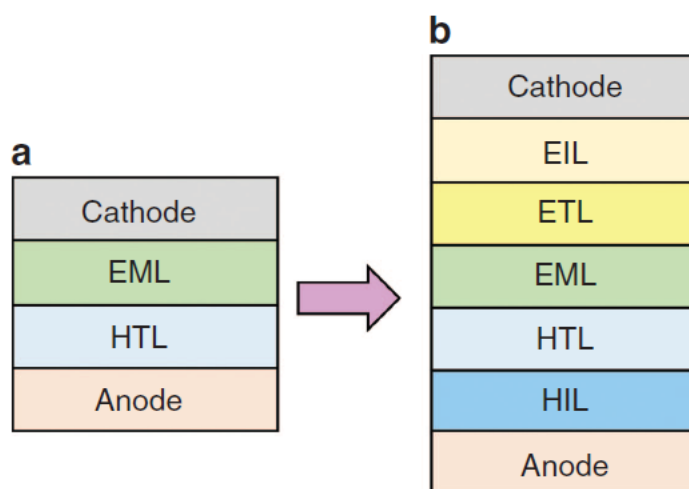## 2.1 Organic Light Emitting Diodes (OLEDs)

Figure 2.1.1 Schematic diagram of an OLED. (a) Basic structure proposed by Tang and Van Slyke in 1987. (b) Multi-layer structure employed in current OLED products. Figure adapted from reference 3.

The basic structure of an efficient, multilayer OLED was first proposed by Tang and Van Slyke in 1987[2]. It consists of two layers of organic thin films, an emission layer (EML) and a hole-transport layer (HTL), inserted between anode and cathode (where the anode layer is located next to the glass substrate layer), as shown in Figure 2.1.1a. Electrons and holes are injected by the electrodes into the organic layers for recombination and light emission. Today, OLEDs multilayer structures with different functional materials are commonly used, as shown in Figure 2.1.1b. The emission layer (EML), which is used for the emission of light, often consists of doping and host materials with high quantum efficiency. The Hole-transport layer (HTL) and the electron-transport layer (ETL) between the EML and the electrodes carry holes and electrons into the EML for recombination. The holes and electron-injection layers (HIL and EIL) are inserted between the electrodes and the HTL and ETL interface to facilitate the injection of the carriers from the conductors to the organic layers through an energy level cascade. When voltage is applied to the OLED, the electrons and holes provided by the cathode and anode, respectively, migrate to the EML for recombination to give an excited species which decays to the ground state by emitting light[1].
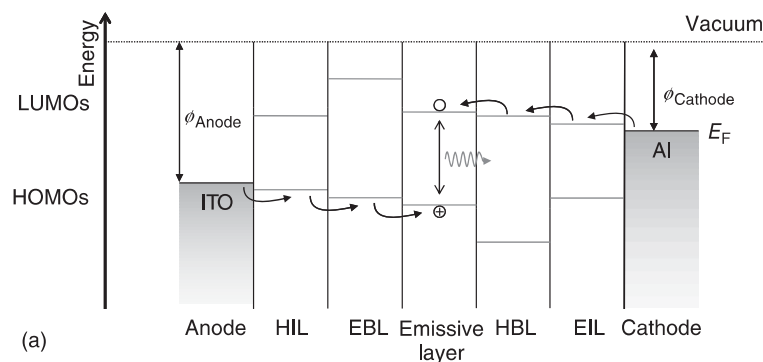
Figure 2.1.2 Example of multilayer device structure at open circuit condition, comprising a hole-injection layer (HIL), an electron-blocking layer (EBL), and an electron-injection layer (EIL) in addition to anode and cathode. The high barriers for hole and electron in the corresponding blocking layers confine changes to the emissive layer, where radiative recombination takes place. Figure adapted from reference 19.

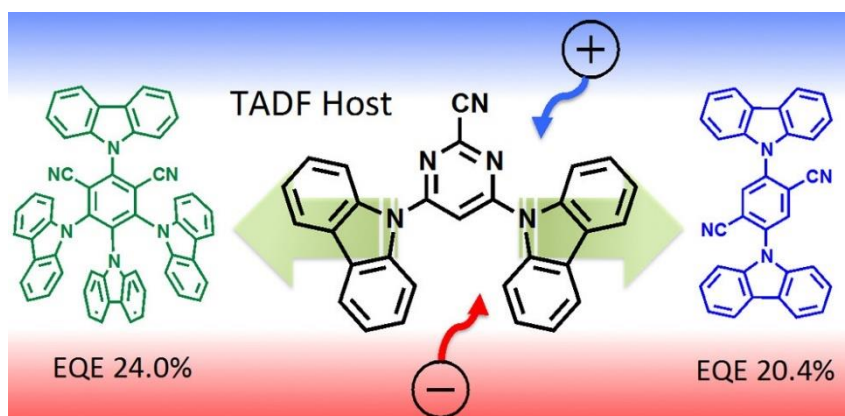## 2.2 Carbazole-based materials as TADF emitters

Figure 2.2.1 Cyanopyrimidine-Carbazole derivative for hybrid host material for high external quantum efficiency of TADF-based OLEDs emitter where 4CzIPN is a green emitter (left) and 2CzIPN is a blue emitter (right). Figure adapted from reference 20.

Carbazole has been widely used in optoelectronic device applications as a source of host and emitter materials[21]. It is an excellent hole-transporter, and also a good electron transporter when functionalized with electron withdrawing groups. Moreover, carbazole has been widely used as an inexpensive starting organic material in the optoelectronic device industry. It also contains a nitrogen atom which facilitates chemical functionalization and therefore modification of properties without altering the backbone, as well as the connection positions on 2, 3, 6, 7 on the carbazole backbone. In addition, its aromatic properties confer chemical stability in a wide range of conditions.

2.3 Singlet and Triplet states

In organic molecules, the electronic ground state is generally a singlet state in which two electrons occupy a single orbital and have coupled antiparallel spins. In excited states, an electron is

promoted to an orbital with higher energy, bringing to a configuration with two unpaired electrons into two different orbitals, either with antiparallel spin (singlet states) or parallel (triplet states). In an electroluminescence process, excited molecules in the emission layer of an OLEDs are generated through a recombination of injected electrons and holes. Since necessarily both holes and electrons have unpaired spins, their combination can originate a singlet or a triplet exciton[4]. According to quantum mechanics, the angular momentum of spin **S** is a vector quantity, sum of all the individual spins of electrons, while the multiplicity of spins (m, the number of possible states for a given value of S, corresponding to different orientations in space) is given by m=2S+1. A two-electron system will obtain four possibilities (Figure 2.3.1), a combination of antiparallel spin, giving a singlet (S=0, m=1), and three parallel spin configurations, i.e. a triplet (S=1, m=3). Therefore, because of the spin statistics, only 25 % of the excitons formed in an OLED are represented by emissive singlets, and 75 % by non-emissive triplets.

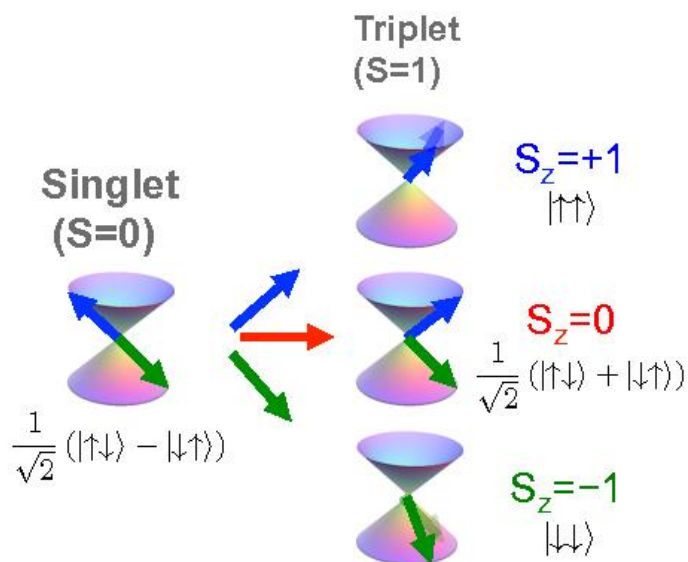**Figure 2.3.1** Spin statistics of a 2-electron system where the first spin wavefunction has S = 0 and m=1. The other three spin wavefunctions have S = 1 and m = 3. They only differ in the z-component of the spin, which can take one of three orientations (S_z = 1, 0, -1).
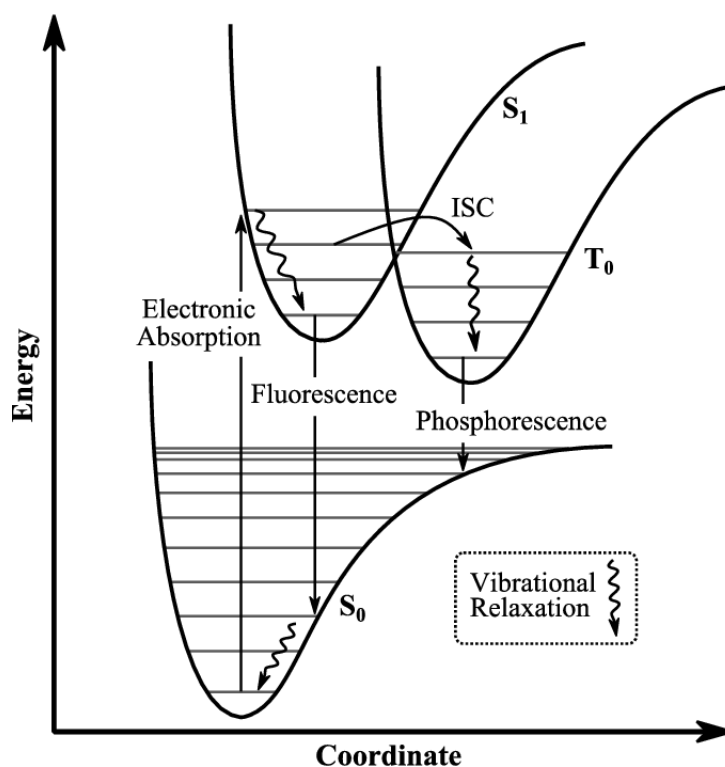
2.4 Frank-Condon principle

Figure 2.4.1 Potential energy diagrams with vertical transitions (Franck–Condon principle).

The Franck–Condon principle is a rule in spectroscopy and quantum chemistry which explains the intensity of vibronic transitions. The basis of this principle is that an electronic transition is very likely to occur without changes in the positions of the nuclei in the molecular entity and its environment. The resulting state is called a Franck–Condon state, and the transition is called the vertical transition. At room temperature, the molecule starts in the vibrational level $v = 0$ of the ground electronic state; after absorbing a photon with the necessary energy, a transition occurs to the excited electronic state. The electron configuration of the new state may involve a shift in the equilibrium position of the nuclei representing the molecule as shown in figure 2.4.1. In the excited electronic state molecules relax quickly at the lowest vibrational level of the lowest electronic excitation state through vibrational relaxation as shown in figure 2.4.1 and in the Jablonski diagram of figure 2.4.2, and from this, they can decay towards the electronic ground state by photon emission. The width of a band in the absorption spectrum is the result of two effects: homogeneous broadening (Lorentzian-shaped) and inhomogeneous broadening. The homogeneous broadening is due to the existence of a continuous series of vibrational sublevels in each electronic state. Inhomogeneous (Gaussian) broadening in liquids results from the fluctuations in the structure of the solvation shell surrounding the chromophore[22], while in solids it arises from some particles having a different local environment from others, and therefore emitting at a different frequency.
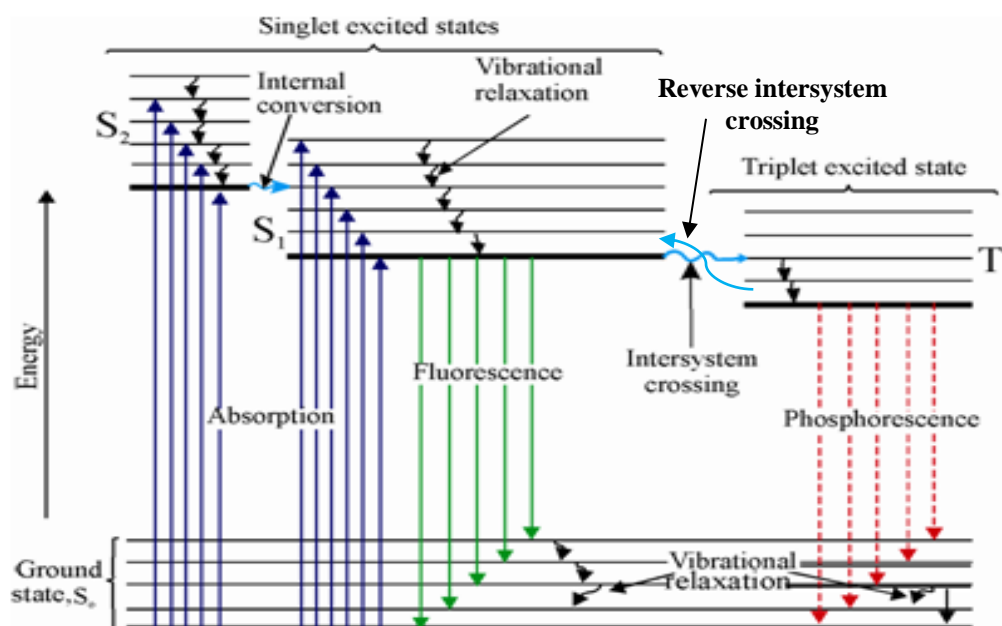
Figure 2.4.2 Jablonski diagram of the energy levels within a molecule showing valence excitations.

2.5 Transition between electronic states

In electronic transitions, selection rules provide the probability of a transition. The rules of selection between electronic states can be related to the oscillator strength (f), which is a dimensionless quantity, proportional to the probability of absorption or emission of electromagnetic radiation. The oscillator strength for specific absorptions can be measured experimentally from the peaks of absorption spectrum as $f = \frac{4.39 \times 10^9}{n} \int \varepsilon(\bar{v}) d\bar{v}$, where $\bar{v}$ is the wavenumber in cm^{-1}, $\varepsilon(\bar{v})$ is the molar extinction coefficient and n is the refractive index of the medium. In turn f is proportional to the square of the transition dipole moment $\boldsymbol{\mu}_{if}$: $f = 4.7 \times 10^{29} \langle \bar{v} \rangle |\boldsymbol{\mu}_{if}|^2$. The transition moment $\boldsymbol{\mu}_{if} = \langle \psi_f | e\boldsymbol{r} | \psi_i \rangle$ can be readily calculated with electronic structure methods, where $e\boldsymbol{r}$ is the dipole moment operator and ψ_f and ψ_i are the spin-electronic wavefunctions of the final and initial states involved in the transition.

2.5.1 The parity

Laporte's rule states that the initial and final wavefunctions must be different to maintain parity, both symmetry and anti-symmetry with respect to an inversion center. For example, g → g or u→ u is forbidden. The allowed transitions must involve a change of parity, g → u or u → g. In addition, the transition π→ π* is allowed since the bonding (π) and anti-bonding (π*) orbitals do not have the same parity.

2.5.2 The spin

The spin rule states that the spin quantum number of the initial and final state must be the same ($\Delta S = 0$). Optical transitions with change in spin multiplicity, such as phosphorescence (PH) are then forbidden ($\boldsymbol{\mu}_{if} = 0$ and $f = 0$), however this rule is broken by spin-orbit coupling (SOC).

2.5.3 Orbital symmetry

The two orbitals involved in a transition must have large amplitudes in the same region, otherwise the transitions are "overlap forbidden". For example, a transition $\pi \rightarrow \pi^*$ is allowed because their orbital is on the same plane and has a high degree of spatial overlap. On the other hand, a transition $n \rightarrow \pi^*$ is forbidden since the lone pair of the n orbitals are typically on the molecular plane and orthogonal to the p orbitals forming the π system.

2.6 Intersystem Crossing and Reverse Intersystem Crossing

In OLEDs, the T_1 state is usually below the S_1 state, a statement that is strictly true is the absence of medium and solvent effects, i.e. in the gas phase. The process of converting a singlet excited state to a triplet excited state is called Intersystem Crossing (ISC). The probability of this process occurring is higher when the vibrational levels of two excited states overlap, since little or no energy needs to be gained or lost during the transition and the geometrical reorganization that follows. ISC is a non-radiative, diabatic process that occurs between states of different multiplicity. The ISC for S_1 can occur from the zero-point vibrational level or from a higher vibrational level of S_1 thermally or radiatively populated (the latter situation is referred to as "hot exciton"). The electron is transferred to the nearby triplet state closer in energy, either T_1 or T_n. Since transitions between states of different spin multiplicity are forbidden, they become partially allowed only if there is a substantial spin-orbit coupling (SOC) between the states[23].

The reverse process, namely the transformation of a triplet excited state into a singlet excited state, is not surprisingly called Reverse InterSystem Crossing (RISC) as shown in figure 2.4.2, and plays an important role in the TADF mechanism. Since the S_1 state is higher in energy than the T_1 state, the energy difference ΔE^{ST} must be small in order to be overcome by thermal fluctuations[24]. Therefore, ΔE^{ST} acts as the activation energy, or part of it (see below), for the RISC process.

2.7 Origin of Singlet and triplet energy splitting

The energy splitting ΔE^{ST} is then a fundamental parameter in the management of the Thermally Activated Delayed Fluorescence process. Three energy terms are considered to calculate the energy of the lowest excited state: orbital energy (E_{orb}), electron repulsion energy (K) and exchange energy (J). The orbital energy term ($E_{orb}<0$) describes the energy associated with the one-

electron orbital in excited state, while the Coulombic "classical" correction of the first order is expressed by the of electron repulsion energy ($K>0$). The exchange energy term ($J>0$) describes the first order quantum-mechanical correction involving electron-electron repulsion due to the Pauli principle, for two electrons residing in the same region of space[13]. The energies of the singlet and triplet states are provided in equation 2.7.1 and 2.7.2 respectively. Due to the different spin of singlet and triplet excited states, the exchange term J increases the energy in S_1 state and decreases that in the T_1 state by the same amount.

$$E_{S1} = E_{orb} + K + J \qquad (2.7.1)$$

$$E_{T1} = E_{orb} + K - J \qquad (2.7.2)$$

$$\Delta E_{ST} = E_{S1} - E_{T1} = 2J \qquad (2.7.3)$$

According to equation 2.7.1 and 2.7.2, the singlet-triplet energy gap is given by 2.7.3. Therefore, ΔE^{ST} depends on the exchange energy, which is related to the excited state and the wavefunctions of the ground state overlap, or more precisely can be different from zero only if the functions $\phi(r)$ and $\psi(r)$ in equation 2.7.4 are simultaneously nonzero at a certain r:

$$J = \iint \phi(r_1)\psi(r_2)(\frac{e^2}{r_1-r_2})\phi(r_2)\psi(r_1)dr_1dr_2 \qquad (2.7.4)$$

where, in a one-electron representation, ϕ and ψ are defined respectively as wavefunctions of HOMO and LUMO, $r_1 - r_2$ is the distance between the electrons in the two orbitals, and e is the electron charge.

For a first order approximation, the exchange interaction is scaled down exponentially with the spatial overlap of the respective electron wavefunctions. If the electron wavefunctions in HOMO and in LUMO superimpose significantly ($\phi(r)\psi(r) \neq 0$ in some regions of the molecule), a large exchange energy $2J$ will be obtained in the order of 0.7-1.0 eV. Smaller exchange energies, in the range between $0.2 - 0.5$ eV, occur in the molecules where HOMO and LUMO are located on different parts of the molecule: this corresponds to the case in which the transitions $S_0 \rightarrow S_1$ and $S_0 \rightarrow T_1$ have at least a partial CT character.

2.8 Spin orbit coupling

As discussed later in this chapter, the RISC rate plays a crucial role in the TADF process. In the Condon approximation, the k_{RISC} between a singlet and a triplet state with wavefunctions ψ_S and ψ_T can be described in equation 2.8.1 using Fermi's golden rule:

$$k_{RISC} \propto |\langle\psi_T|\hat{\mathcal{H}}_{SOC}|\psi_S\rangle|^2 \sum_{k,j} |\langle v_{Tk}|v_{Sj}\rangle|^2 \qquad (2.8.1)$$

where υ are the vibrational energy level and $\hat{\mathcal{H}}_{SOC}$ is the spin-orbit Hamiltonian. It is clear that, regardless of vibrational motions, RISC rate is driven by the spin-orbit coupling $\langle \psi_T | \hat{\mathcal{H}}_{SOC} | \psi_S \rangle$[25]. Spin orbit coupling (SOC) is a relativistic interaction that depends on the magnitude and mutual orientations of electron orbital and spin angular momenta, and that leads to the fine-structure splitting of the system energy levels in presence of magnetic fields.

In the high-temperature regime, the overlap between singlet and triplet vibrational states $\sum_{k,j} |\langle \upsilon_{Tk} | \upsilon_{Sj} \rangle|^2$ shows an Arrhenius-type temperature dependence, and the rate assumes the classical expression:

$$k_{RISC} = A \cdot \exp(-\frac{\Delta E_{ST}}{kT}) \tag{2.8.2}$$

where k is the Boltzmann constant, T is the temperature, and the prefactor A is proportional to the square SOC electronic coupling $V_{SOC}^2 = |\langle \psi_T | \hat{\mathcal{H}}_{SOC} | \psi_S \rangle|^2$.

If on the other hand, we consider coupling with an effective classical vibrational mode, the RISC rate can be expressed, in the semi-classical Marcus theory, as[26]:

$$k_{rISC} = \frac{2\pi}{\hbar} V_{SOC}^2 \frac{1}{\sqrt{4\pi \lambda kT}} \exp\left[-\frac{(\lambda + \Delta E_{ST})^2}{4\lambda kT}\right] \tag{2.8.3}$$

where the reorganization energy $\lambda = \lambda_{out} + \lambda_{in}$ contains (classical) contributions of the low-frequency modes for the surrounding medium λ_{out} and high-frequency intramolecular vibrational modes λ_{in}. Accounting for reorganization, the activation energy in eq. 2.82. then becomes $\frac{(\lambda + \Delta E_{ST})^2}{4\lambda}$.

An practical strategy to improve the intensity of SOC is the so-called heavy-atom effect, i.e. the insertion of heavy atoms (transition metal) in the organic structure, efficiently exploited in popular Iridium-based phosphorescent emitters[23]. However, purely organic materials tend to have weaker spin-orbit coupling, which means that the spin-flip mechanism of ISC and RISC is not efficient. In this case to obtain a relatively high ISC and RISC rate without heavy metal atoms, a small ΔE^{ST} can speed up the process, provided that V_{SOC} is not null. This is often measured from the value of a first-order mixing coefficient (γ) between the excited state of singlet and triplet[27,28].

$$\gamma \propto \frac{V_{SOC}}{\Delta E_{ST}} \tag{2.8.4}$$

From equations 2.8.2-2.8.4 it follows that heavy atoms are not required to obtain an efficient spin conversion when a molecule has a small ΔE^{ST}, and V_{SOC} is not frustratingly small.

2.9 Internal quantum efficiency in presence of Delayed Fluorescence

Delayed fluorescence occurs when a molecule in the T_1 state goes through a slow transition to the S_1 state followed by a radiative transition to S_0, which results in an emission identical in wavelength to fluorescence, but which occurs on a longer time scale. Delayed fluorescence occurs through two distinct mechanisms: thermally activated delayed fluorescence (also known as E-type[22]) and triplet-triplet annihilation (a bimolecular process known as P-type). In this context, only details on TADF will be provided.
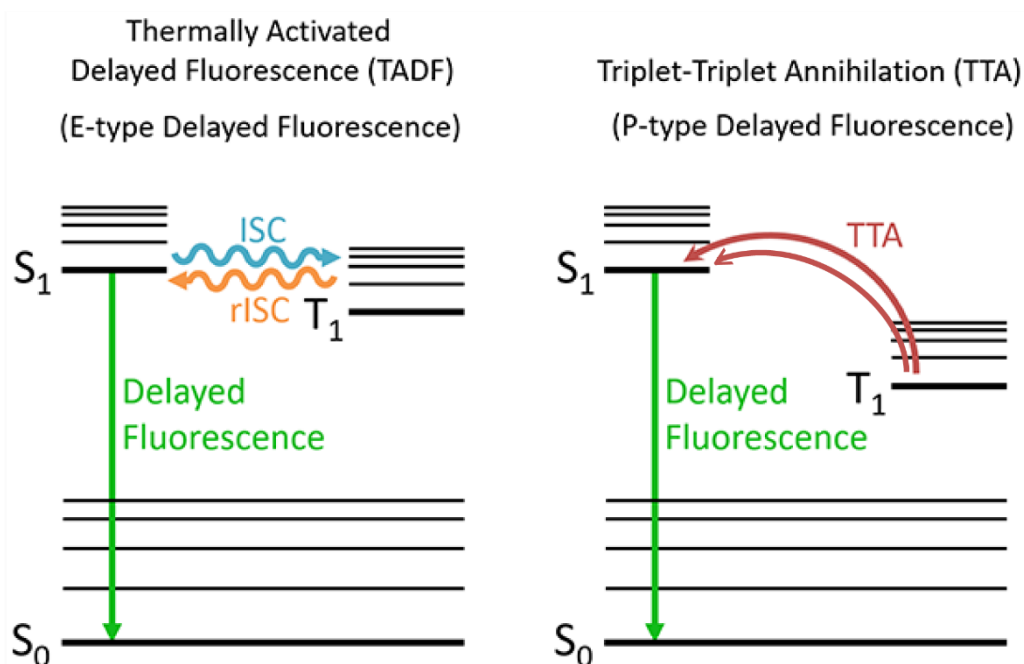

Figure 2.9.1 Mechanism of delayed fluorescence: Thermally Activated Delayed Fluorescence (left) and Triplet-Triplet Annihilation (right)

As already mentioned, thermally activated delayed fluorescence (TADF) is the process in which the molecule transits from the T_1 state to the S_1 state through reverse intersystem crossing (RISC) and then emits. Recent studies of TADF based-OLED have achieved internal quantum (IQE) efficiency of almost 100 %, which for simplicity we describe here with equation 2.9.1. In TADF-based OLEDs, the IQE, i.e. the ratio between the photons emitted and the excitons produced, therefore derives from several electronic processes: prompt fluorescence (PF), delayed fluorescence (DF), and direct and reverse intersystem crossing (ISC, RISC)[12]. To obtain high efficiency, the photoluminescence quantum yield of PF ($\emptyset_{PF}$) and of DF ($\emptyset_{DF}$) should be maximized as suggested by the following equation:

$$\eta_{int} = n_{r,S}\emptyset_{PF} + n_{r,S}\emptyset_{DF} + n_{r,T}\frac{\emptyset_{DF}}{\emptyset_{ISC}} \qquad (2.9.1)$$

where η_{int} is the IQE, $n_{r,S}$ is the generation efficiency of the singlet exciton (0.25), $n_{r,T}$ is the production of the triplet exciton (0.75), $\emptyset_{ISC}$ is the quantum yield of singlet to triplet intersystem crossing (inversely proportional to that RISC). Obviously, high IQE in TADF based-OLEDs emitters can be reached with high $\emptyset_{PF}$, high $\emptyset_{DF}$ and low $\emptyset_{ISC}$ (high $\emptyset_{RISC}$) values. The $\emptyset_{PF}$ can be enhanced by efficient fluorescence process while $\emptyset_{DF}/\emptyset_{ISC}$ can be maximized by minimizing the singlet-triplet energy gap splitting as shown in equation 2.9.2 which exploits eq. 2.8.2 and introduces a non-radiative decay process with rate k_{nr} in competition with RISC.

$$\frac{\emptyset_{DF}}{\emptyset_{ISC}} = \frac{1}{1+\dfrac{k_{nr}}{\emptyset_{PF}A\exp(-\frac{\Delta E_{ST}}{kT})}} \qquad (2.9.2)$$

2.10 Summary of experimental results for 5CzBN

The experimental work from Adachi and co-workers shows that 5CzBN has a $\Delta E^{ST} = 0.17$ eV which is a bit too large to achieve high efficiency RISC at room temperature. Nevertheless, it shows a high external quantum efficiency (EQE) = 24 % and emitting in blue region. The role of triplet states in the delayed emission is demonstrated by the observation than all the molecules are TADF-inactive in presence of O_2 in toluene (O_2 is a very efficient triplet quencher, figure 2.10.1).
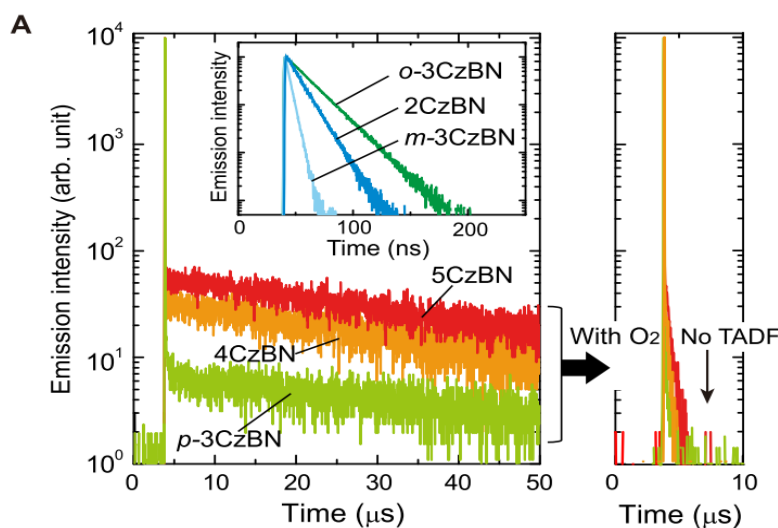

Figure 2.10.1 Photoluminescence decay curve of CzBN derivatives in toluene at 298 K where 5CzBN shows both prompt fluorescence and delayed fluorescence (left), and TADF quenching by molecular oxygen (right). Figure adapted from reference 18.

These data imply that, to achieve high rate of RISC, a $\Delta E^{ST} = 0.17$ eV does not play a major role. The authors of ref. 18 postulated that the formation of a delocalized CT state is the key to promote a large k_{RISC} even when the energy-splitting of S_1 and T_1 is not close to zero. They also

16

pointed out the importance of the restriction of structure relaxation in the T_1 state to achieve a high photoluminescent efficiency. Linearly positioning of carbazole pairs connected with respect to the benzonitrile unit may cause the structure relaxation, depending on the free space around the carbazoles, to deactivate the T_1 state. As a result, they proposed the structure to form delocalized CT by keeping it rigid, i.e. by introducing bulky moieties around the donor unit in a D-A-D structure. In the following, we will test these speculations by comparing p-2CzBN, in which carbazole rotation is not restricted, with 5CzBN in which on the contrary there is strong restriction and steric hindrance.
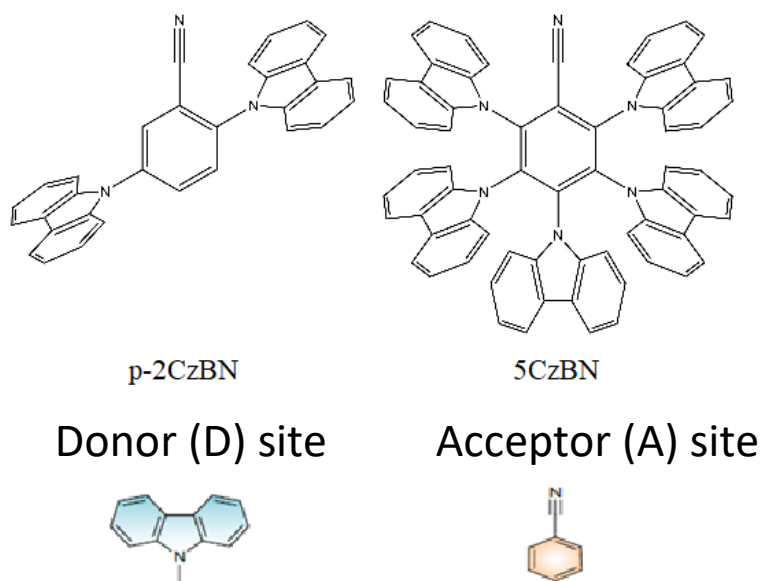

Figure 2.10.2 Molecular structure of 2,5-di(9*H*-carbazol-9-yl)benzonitrile (p-2CzBN) and 2,3,4,5,6-penta(9*H*-carbazol-9-yl)benzonitrile (5CzBN) where carbazole is a donor group and benzonitrile an acceptor group.

Chapter 3

Electronic structure of p-2CzBN and 5CzBN

Two molecules, namely 2,5-di(9*H*-carbazol-9-yl)benzonitrile (p-2CzBN), and 2,3,4,5,6-penta(9*H*-carbazol-9-yl)benzonitrile (5CzBN), which exhibits TADF[18], were selected to characterize their ground and excited state properties, looking for a deeper understanding of the effect of their donor-acceptor (D-A) and donor-acceptor-donor (D-A-D) structures, on the efficiency of reverse intersystem crossing (RISC). As mentioned in Chapter 2, Carbazole (Cz) plays the role of electron donating (D) group, while benzonitrile (BN) is the electron accepting (A) group. In this section we compare the potential energy surfaces of the two molecular architectures, also as a function of Cz-BN dihedral angles, with a combination of DFT calculations for the ground state and Tamm-Dancoff approximation (TDA) calculations for excited state.

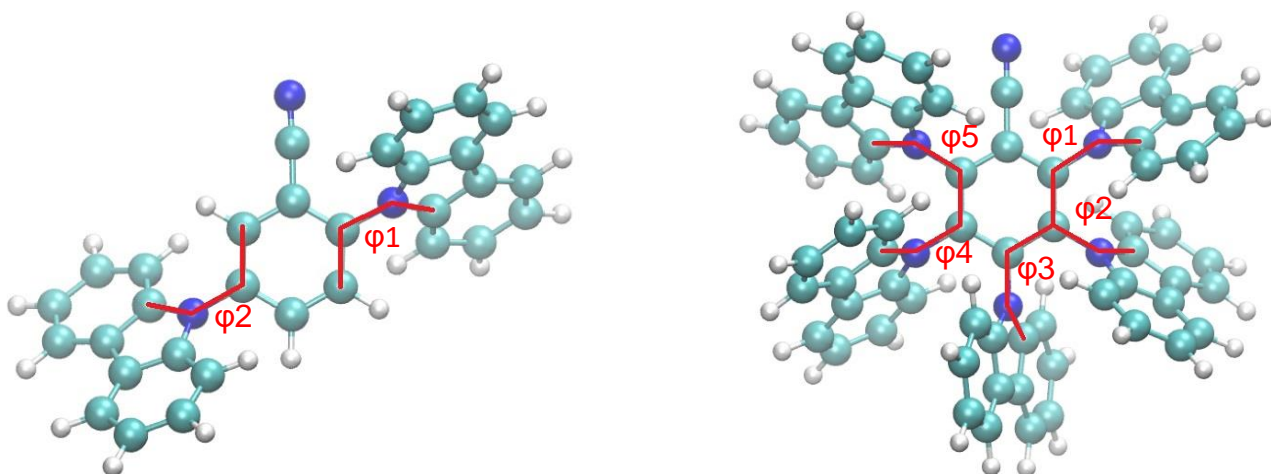## 3.1 Geometry optimization of p-2CzBN and 5CzBN

Figure 3.1.1 The PBE1PBE/6-31G** optimized structure of p-2CzBN (left) and 5CzBN (right)

The geometrical and electronic properties of p-2CzBN and 5CzBN were first calculated with the Gaussian 16 program package. The ground state (S_0) of p-2CzBN was first optimized by means of DFT calculations with the PBE1PBE hybrid functional with the moderate basis set 6-31G**, then the calculation was improved with the 6-311G** and cc-pVTZ basis set. The optimized structures were used to compute the vibrational frequencies in order to check the structural stability[29]. No imaginary frequencies are found as expected for a geometry corresponding to an absolute minimum of the PES. The optimized structures of p-2CzBN and 5CzBN are shown in figure 3.1.1, where the carbazole-benzonitrile dihedral angles used in the potential energies scan, described in the following, are also defined. The calculated equilibrium values of dihedral angles at PBE1PBE/6-31G** level were $\varphi_1 = 56.0°$ and $\varphi_2 = 51.6°$ for p-2CzBN, and $\varphi_1 = 64.7°$, $\varphi_2 = 61.3°$, $\varphi_3 = 59.8°$, $\varphi_4 = 61.3°$ and

$\varphi_5 = 64.7°$ for 5CzBN, with small variations at increasing the basis set. Due to the symmetry of the carbazole substituent, we only studied the torsion from 0° to 180° assuming the same effect from 0° to -180°, and used in all the calculations the smaller 6-31G** basis. The molecular symmetry of p-2CzBN therefore gave two minima points in the whole scan from 0° to 180°, at 60° and at 120° for φ_1 and at 50° and at 130° for φ_2. We found that also for 5CzBN structures with φ_1 and φ_2 equal to 60° are nearly equivalent in energy to the structures with φ_1 and φ_2 equal to 120°. All the gas phase optimization results are given in table 3.1.

Table 3.1 Calculated ground state (S_0) energy (Hartree) and dihedral angles (deg) of p-2CzBN and 5CzBN at the optimized geometry.

| Molecule	Functional/basis set	φ_1	φ_2	φ_3	φ_4	φ_5	Optimized energy
p-2CzBN	PBE1PBE/6-31G**	56.0	51.6	-	-	-	-1355.4923
		60.0	50.0	-	-	-	-1355.4922
		120.0	130.0	-	-	-	-1355.4922
	PBE1PBE/6-311G**	57.5	53.2	-	-	-	-1355.7412
	PBE1PBE/cc-pVTZ	57.7	55.1	-	-	-	-1355.8748
5CzBN	PBE1PBE/6-31G**	64.7	61.3	59.8	61.3	64.7	-2902.5400
		60.0	61.3	59.8	60.0	64.8	-2902.5399
		120.0	-60.6	-60.0	120.0	-63.8	-2902.5398
	PBE1PBE/6-311G**	63.7	60.7	59.2	60.7	63.8	-2903.0664
	PBE1PBE/cc-pVTZ	66.2	61.9	60.4	61.8	66.3	-2903.3479

In table 3.1, we also report the geometries with both dihedral angles fixed to 60° and 120° (or 50° and 130° if dihedral angle was defined with positive value) which also confirmed to be minima of the PES during the torsional energy profile scan, or to be more precise, that the potential energy surface around the minima is very shallow. During the geometry optimization one can reach one of the two minima depending on the initial geometry. Interestingly, for 5CzBN, when φ_1 and φ_4 are fixed to 60° and 120° while letting the φ_2, φ_3, and φ_5 relax, the values of φ_1 and φ_4 do not change much. Therefore, for simplicity we will only compute the potential energy scan of 5CzBN with respect to only 2 dihedral angles (either φ_1 and φ_4, or the φ_2 and φ_5 letting the other two at their equilibrium values). We assume that the variation of the other two dihedrals would bring the same, additive variation of any electronic property.

3.2 Frontier orbitals characterization

We then investigated the shape and energy of frontier molecular orbitals at the equilibrium geometry. As expected, carbazole moieties appear to be the donor group, hosting the occupied molecular orbital with highest energy (HOMO), while benzonitrile behave as acceptor group hosting the lowest energy unoccupied orbital (LUMO): p-2CzBN and 5CzBN actually correspond to D-A and D-A-D architecture. Figure 3.2.1 shows that for p-2CzBN, the HOMO is mainly localized on the carbazole group in position 2, while the LUMO is localized on benzonitrile. For 5CzBN, the LUMO is localized on four benzonitrile group, in position 2,3,5,6, but the HOMO is more delocalized with respect to its p-2CzBN counterpart, with some density on the carbazole group in position 4. The energy separation between HOMO and LUMO of p-2CzBN and 5CzBN are 4.11 eV and 3.73 eV, respectively. This suggests that p-2CzBN should possess a slightly larger optical gap than 5CzBN, consequently p-2CzBN absorption/emission should be blue-shifted with respect to that of 5CzBN. We also note that both p-2CzBN and 5CzBN have frontier orbitals rather close in energy to HOMO (HOMO-1 as shown in figure 3.2.2).
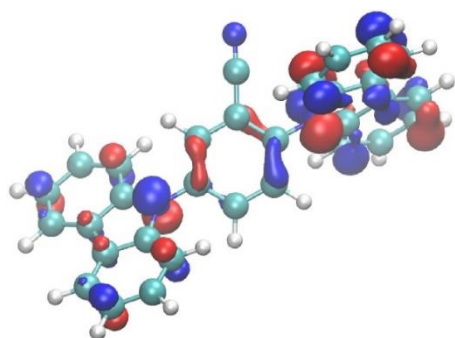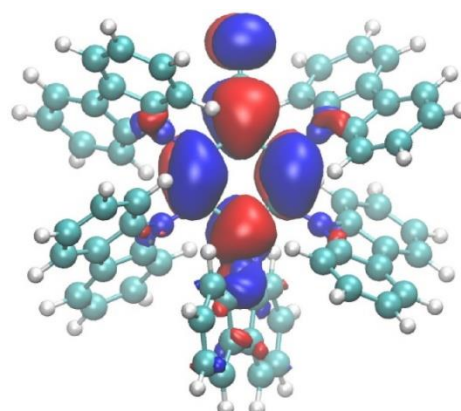
Homo (-5.84 eV)
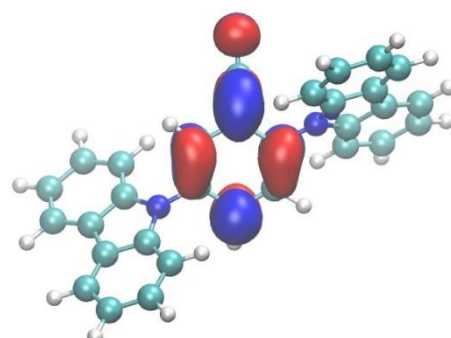
Lumo (-1.73 eV)
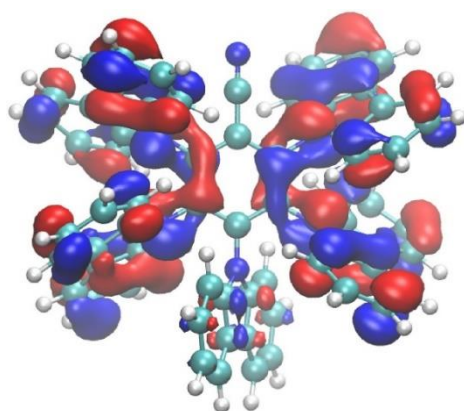
Homo (-5.79 eV)

Lumo (-2.06 eV)

Figure 3.2.1 Isocontour plots (cutoff=0.04 a.u for p-2CzBN and 0.02 a.u for 5CzBN.) of frontier orbitals (HOMO and LUMO) of p-2CzBN (top) and 5CzBN (bottom) calculated at the PBE1PBE/6-31G** (at the equilibrium geometry).

Homo-1 (-6.10 eV)   Lumo+1 (-1.12 eV)

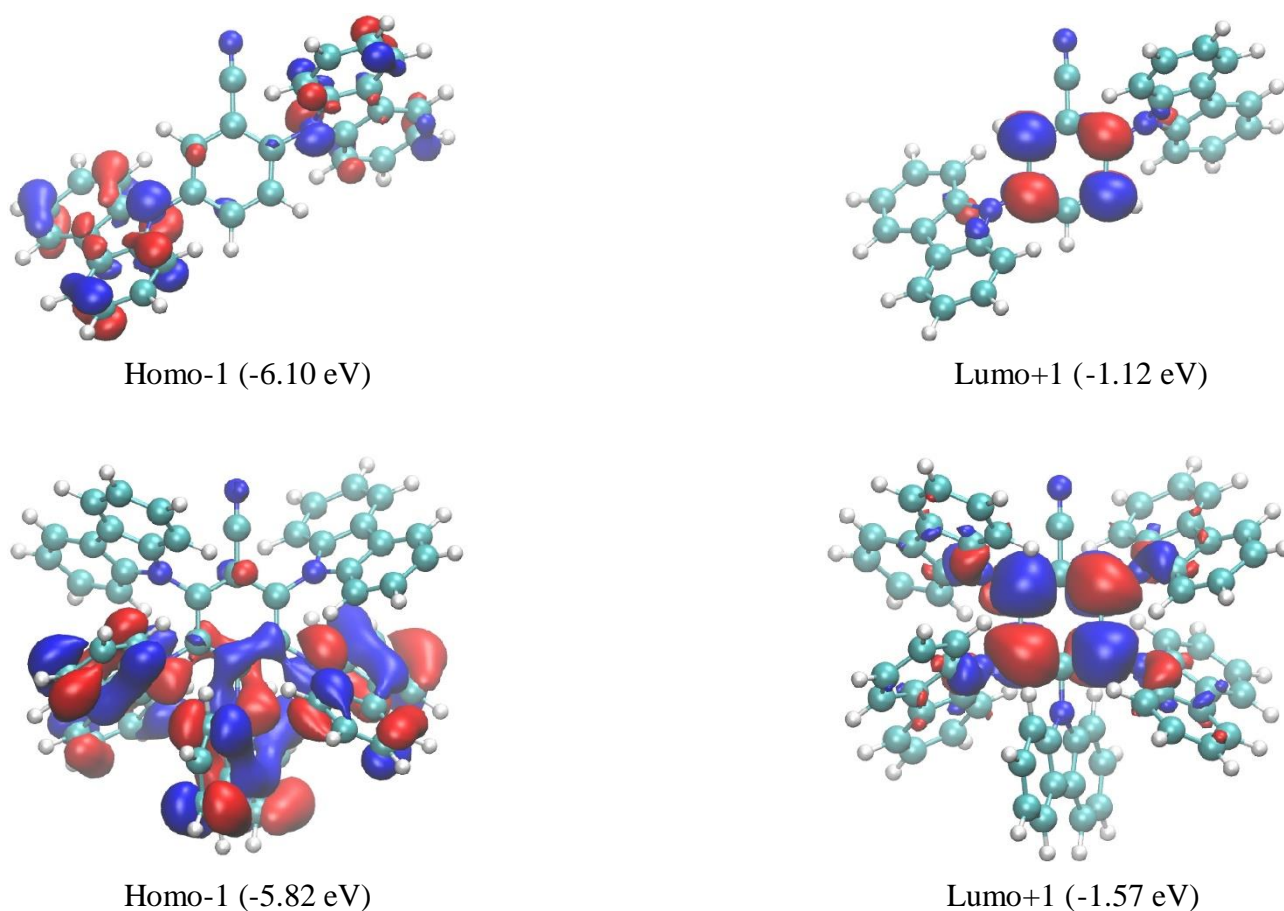Homo-1 (-5.82 eV)   Lumo+1 (-1.57 eV)

Figure 3.2.2 Isocontour plots (cutoff = 0.04 a.u for p-2CzBN and 0.02 a.u for 5CzBN.) of frontier orbitals (HOMO-1 and LUMO+1) of p-2CzBN (top) and 5CzBN (bottom) calculated at the PBE1PBE/6-31G** (at the equilibrium geometry).

The difference in energy of HOMO and HOMO-1 of p-2CzBN and 5CzBN are 0.26 eV and 0.03 eV respectively. The LUMO and LUMO-1 orbital shape 5CzBN are very similar, while for 2CzBN HOMO-1 is still similar but more delocalized into the benzonitrile ring. While for HOMO and HOMO-1 there is a delocalized in both molecules on carbazoles, in particular the delocalized for HOMO is concentrated on the carbazole closest to the cyan group while for HOMO-1 it is concentrated on more distant carbazole. In the table 3.2 are given the energies of all the frontier orbitals that are relatively close to HOMO and LUMO, calculated not only in gas phase but also in toluene with the polarizable continuum model (PCM). Toluene, the solvent used in UV/VIS experiments in reference[18], appears to slightly stabilize all the orbital energies without altering the general trend.

Table 3.2 Frontier molecular orbital energies of p-2CzBN and 5CzBN as obtained with the level of calculation PBE1PBE//6-31G** in gas phase and with implicit solvation model for toluene (PCM model, $\varepsilon = 2.3741$).

Molecular orbital	Orbital Energy (eV)			
	p-2CzBN		5CzBN	
	Gas phase	PCM	Gas phase	PCM
HOMO-2	-6.187	-6.239	-5.872	-5.975
HOMO-1	-6.097	-6.099	-5.816	-5.893
HOMO	-5.837	-5.857	-5.793	-5.885
LUMO	-1.733	-1.739	-2.061	-2.173
LUMO+1	-1.117	-1.075	-1.567	-1.649
LUMO+2	-0.890	-0.877	-0.765	-0.842

3.3 Excited state calculation of p-2CzBN and 5CzBN

The excited states were calculated using the Tamm-Dancoff approximation (TDA) calculations with PBE1PBE/6-31G** and then improving the calculation accuracy with the larger 6-311G** and cc-pVTZ basis set. The excited energies of triplet and singlet were calculated based on the optimized ground state geometry[30]. The vertical excitation energy was computed for absorption from the ground state S_0 to the first singlet S_1 ($E_V(S_1)$) and triplet T_1 ($E_V(T_1)$) excited-states; the calculation yields correspondingly the vertical singlet–triplet gap as $\Delta E^{ST} = E_V(S_1) - E_V(T_1)$. Since, Adachi and co-workers conducted experiments in toluene for this type of compounds, the solvent effect was included by using the non-equilibrium Polarizable Continuum Model for excited state calculations[11]. For 5CzBN, the state energies and the calculated vertical gap ΔE^{ST} at the minimum energy conformer in the presence of toluene ($\varepsilon = 2.3741$) are compared with the experimental values from Adachi and co-workers[18]. Oscillator strength (f or O.S.) are also given in tables 3.3.1 and 3.3.2. For p-2CzBN results show that the use of 6-311G** and cc-pVTZ basis set gave the energy of vertical singlet–triplet gap slightly lower than the use of 6-31G** basis set, even if the two gaps are similar. More importantly, the vertical energy splitting of singlet and triplet of about 0.30 eV for p-2CzBN and 0.21 eV for 5CzBN (versus an experimental one of 0.17 eV), which are maybe too high to drive an efficient rate of RISC, however despite the nearly equal ΔE^{ST} the TADF performance of the two compounds is completely different. Therefore, the key to drive TADF process in p-2CzBN and 5CzBN should not depend solely on ΔE^{ST} differences, but on other parameters such as the oscillator strength. Indeed, both basis sets gave rather low values for p-2CzBN oscillator strength, and even smaller for 5CzBN, indicating a less efficient light emission for the latter compound. The problem of

small oscillator strength from S_1 to S_0, which eventually leads to low photoluminescence quantum efficiency in TADF based-OLEDs, will be addressed further in this chapter. The comparison between gas phase and solvent calculation, shows values close to experimental results of 5CzBN and higher oscillator strengths in the presence of toluene, for both compounds, possibly indicative of a better performance in solid state with respect to what predicted by gas phase calculations.

Table 3.3.1 Calculated vertical transition energies, singlet-triplet energy gaps, and oscillator strengths (O.S) at the equilibrium geometry of p-2CzBN, calculated in gas phase and in toluene (PCM model, $\varepsilon = 2.3741$). [a]Note that the oscillator strength is only defined for singlet excitation.

Functional/basis set	States	Energy (eV)		O.S[a]	
		Gas phase	PCM model	Gas phase	PCM model
PBE1PBE/6-31G**	S_1	3.3029	3.3045	0.1169	0.1441
	S_2	3.5807	3.5643	0.0039	0.0028
	T_1	3.0040	3.0187	-	-
	T_2	3.4132	3.4149	-	-
	ΔE^{ST}	0.2989	0.2858	-	-
PBE1PBE/6-311G**	S_1	3.2804	-	0.1139	-
	S_2	3.5561	-	0.0032	-
	T_1	2.9856	-	-	-
	T_2	3.3929	-	-	-
	ΔE^{ST}	0.2948	-	-	-
PBE1PBE/cc-pVTZ	S_1	3.2658	-	0.1073	-
	S_2	3.5407	-	0.0023	-
	T_1	2.9718	-	-	-
	T_2	3.3804	-	-	-
	ΔE^{ST}	0.2940	-	-	-

Table 3.3.2 Calculated vertical transition energies, singlet-triplet energy gaps, and oscillator strengths (O.S) at the equilibrium geometry of 5CzBN, calculated in gas phase and in toluene (PCM model, $\varepsilon = 2.3741$). Experimental values from reference 18 are given between round brackets. [a]Note that the oscillator strength is only defined for singlet excitation.

Functional/ basis set	States	Energy (eV)			O.S[a]	
		Gas phase	PCM model	experiment	Gas phase	PCM model
PBE1PBE/6-31G**	S_1	2.9528	2.9271	2.95	0.1041	0.1350
	S_2	2.9760	2.9559	-	0.0420	0.0847
	T_1	2.7382	2.7204	2.78	-	-
	T_2	2.7923	2.7747	-	-	-
	ΔE^{ST}	0.2146	0.2067	0.17	-	-

We also computed the absorption spectrum of p-2CzBN and 5CzBN by using the Tamm-Dancoff approximation (TDA) with PBE1PBE/6-31G** and PCM in toluene. The calculation shows that the spectrum of 5CzBN is red-shifted respect to 2CzBN (figure 3.3.1). This result is corresponding to the different HOMO-LUMO gap in table 3.2 as the energy gap of p-2CzBN is larger than 5CzBN (in agreement with experimental result from Adachi and co-workers[18]).
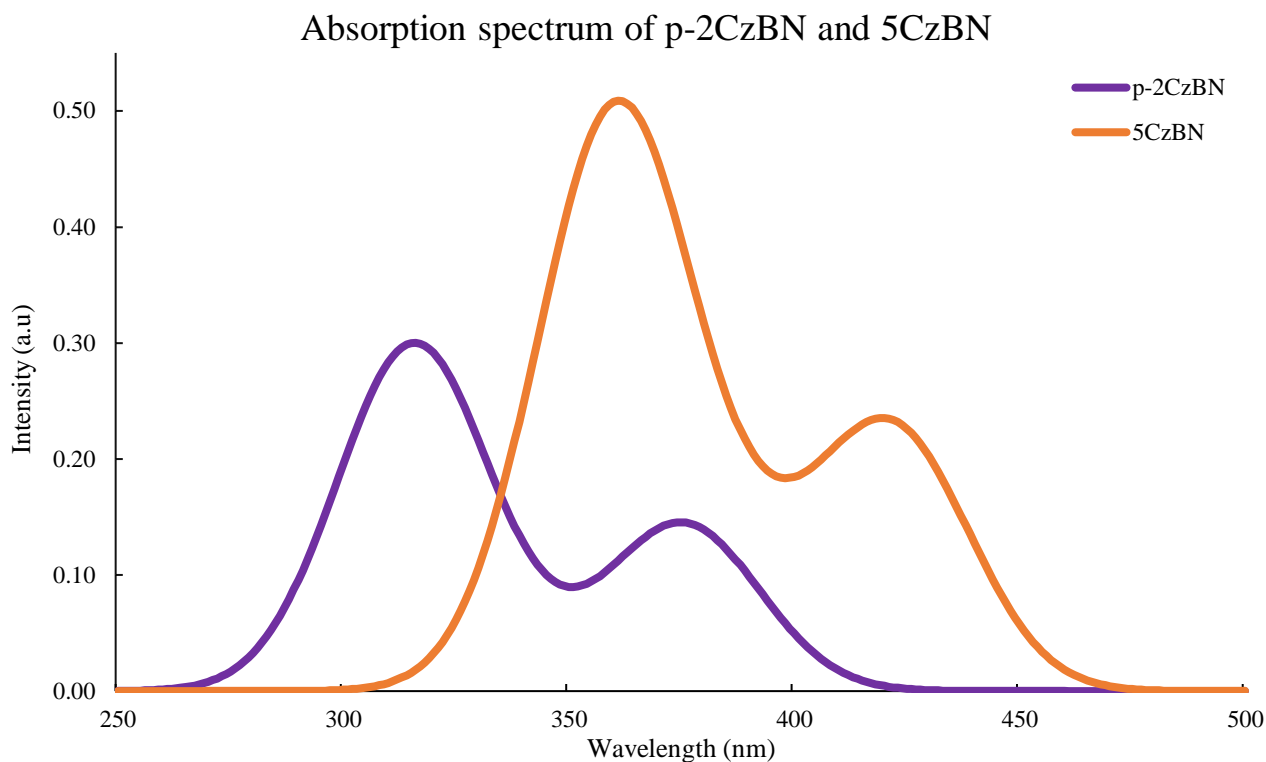

Figure 3.3.1 The absorption spectrum of p-2CzBN and 5CzBN calculated by using TDA-PBE1PBE/6-31G** with the PCM solvation model (Gaussian function: broadening 0.2 eV).

The influence of molecular geometry and the interaction with the solvent provides a possible source of variability in the excitation energy, leading to broadening in the transition from S_1 to S_0 as shown in figure 3.3.1, where a Gaussian broadening of 0.2 eV was applied to the TDA-DFT energies. However, this broadening partially hides that the spectral features arise from the presence of low-lying singlets excited states close in energy. The electronic transitions that are involved in the spectrum of p-2CzBN and 5CzBN are more neatly shown in figure 3.3.2., where a narrow Gaussian broadening was applied. The orbitals contributing to spectrum for each transition of p-2CzBN and 5CzBN with no vanishing oscillator strength are given in table 3.3.3:
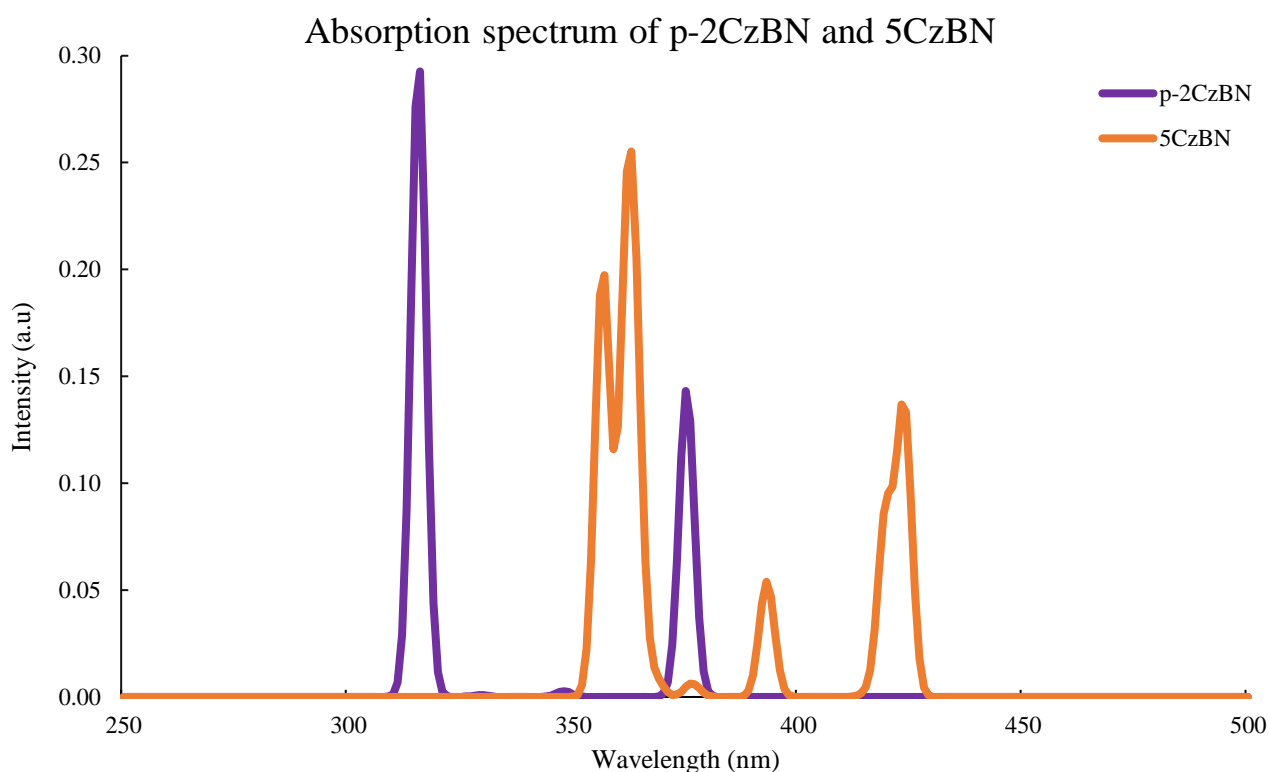

Figure 3.3.2 The absorption spectrum of p-2CzBN and 5CzBN calculated by using TDA-PBE1PBE/6-31G** with PCM model (Gaussian function: broadening 0.02 eV).

The frontier orbitals that mostly contribute to the transition are HOMO-1, HOMO, LUMO and LUMO+1 in p-2CzBN and 5CzBN. The transition from S_0 to S_5 of p-2CzBN has a high oscillator strength (0.296) and corresponds to an excitation energy in the near-UV region. We stress that only 5CzBN is TADF active although it shows a slightly lower oscillator strength than p-2CzBN. This could be one of the reasons that may lead us to think that p-2CzBN could also be a TADF active emitter. Figure 3.3.3 we show instead the dependence on carbazole conformation of the $S_0 \rightarrow S_1$ excitation energy: the variability is larger for p-2CzBN, and the lowest excitation energies are found at ±90°, ±90° , and not at the Franck-Condon points ±60°, ±60° and ±120°, ±120°. 5CzBN shows less

pronounced features but totally opposite, in fact, it shows lower excitation energies more or less at the Franck-Condon points.

Table 3.3.3 Orbitals contributing to spectrum for each transition of p-2CzBN and 5CzBN, calculated in toluene (PCM model, ε = 2.3741). Excitation coefficients, excitation energy (nm) and oscillator strength are also given. The orbital numbers for p-2CzBN are H=HOMO = 113 and L=LUMO =114 and for 5CzBN H=HOMO = 242 and L=LUMO = 243.

|	Transition	Orbital contribution	Coefficient of wavefunction	Excitation energy (nm)	Oscillator strength
p-2CzBN	$S_0 \rightarrow S_1$	H-1$\rightarrow$L	-0.13687	375.20	0.1441
		H$\rightarrow$L	0.68727		
	$S_0 \rightarrow S_5$	H-1$\rightarrow$L+1	0.69338	315.66	0.2964
5CzBN	$S_0 \rightarrow S_1$	H$\rightarrow$L	0.69414	423.58	0.1350
	$S_0 \rightarrow S_4$	H-3$\rightarrow$L	0.67166	393.11	0.0502
		H-2$\rightarrow$L	0.13599		
	$S_0 \rightarrow S_6$	H-5$\rightarrow$L	0.62717	376.36	0.0065
		H-4$\rightarrow$L	-0.31279		
	$S_0 \rightarrow S_8$	H-8$\rightarrow$L	-0.42439	363.75	0.1160
		H-2$\rightarrow$L+1	-0.25521		
		H-1$\rightarrow$L+1	0.47428		
	$S_0 \rightarrow S_{10}$	H-7$\rightarrow$L	-0.33488	361.86	0.0836
		H$\rightarrow$L+1	0.59654		
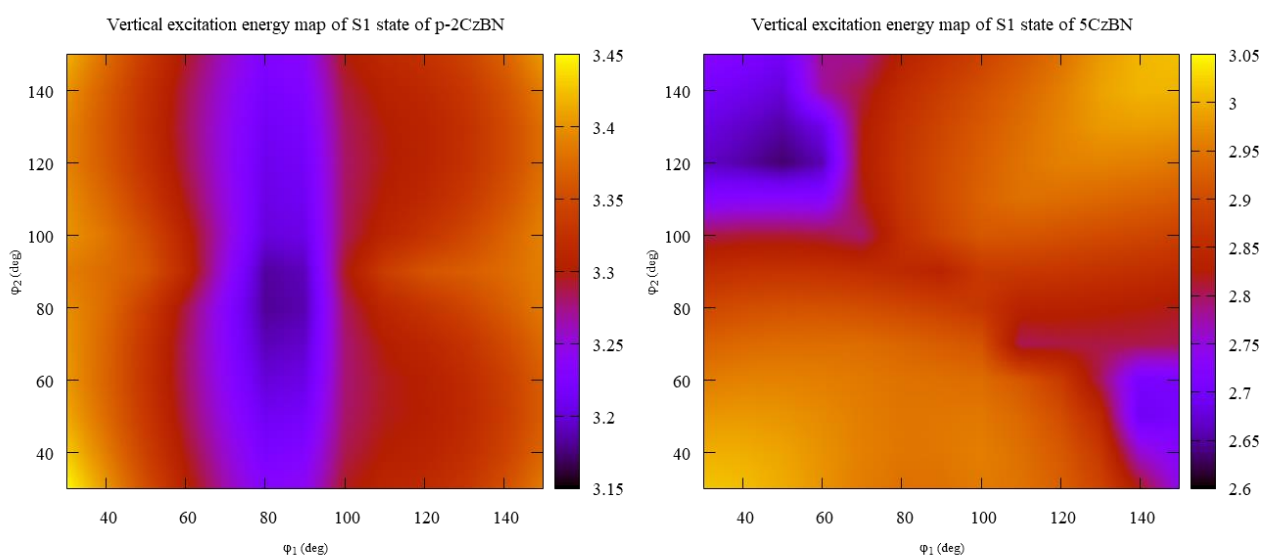
Figure 3.3.3 The vertical excitation energy from $S_0 \rightarrow S_1$ calculated by using TDA-PBE1PBE/6-31G** as a function of the two carbazole-benzonitrile dihedral angles for p-2CzBN (left) and 5CzBN (right).

3.4 Torsional energy profiles of p-2CzBN and 5CzBN

Figure 3.3.3 suggests that the molecular flexibility could have an important effect on the color of the emission. To investigate in greater detail the possible conformations of carbazole groups, the relaxed torsional energy profiles of two carbazole-benzonitrile dihedral angles were calculated. The potential energy surface of p-2CzBN was explored by keeping fixed one dihedral angle φ_1 while letting the other one relax (φ_2) (figure 3.1.1), and vice versa. The dihedral angle was scanned from 0° to 180° (only half of the available range). The other half range (from 0° to -180°) leads to the same potential energy profile because of the symmetry of carbazole group. The scan was calculated first at PBE1PBE/6-31G** level. In figure 3.4.1, it can be seen that the torsional energy profiles of both dihedral angles are similar. The minima points are found at $\pm 60^o$ and $\pm 120^o$ for φ_1, while, for φ_2 the minima points are found at $\pm 50^o$ and $\pm 130^o$, while the saddle point is set at $\pm 90^o$ with a difference in energy of 0.6 kcal/mol. Actually, the profiles should exhibit mirror symmetry with respect to 90°, but they do not at the maxima, due to some hysteresis arising from the orientation of the carbazole of φ_2 which does not change symmetrically during the optimization. In addition, the carbazole in position 5 is much less affected by the presence of the cyano group of benzonitrile because it is more distant than the carbazole in position 1 (φ_1), for this reason the minima points for φ_2 are found at $\pm 50^o$ and $\pm 130^o$. To verify the potential energy profile, the PES of p-2CzBN was then obtained (calculation with respect to PBE1PBE/6-31G** optimized conformations) with a bigger basis set (6-311G** and cc-pVTZ,). We have compared the basis sets 6-31G** with 6-311G** and cc-pVTZ, observing that they lead to similar relative energies. Then we opted for using the moderate basis set (6-31G**) to obtain the PES of 5CzBN, which is a bigger molecule and consequently more demanding in terms of time and computational cost.
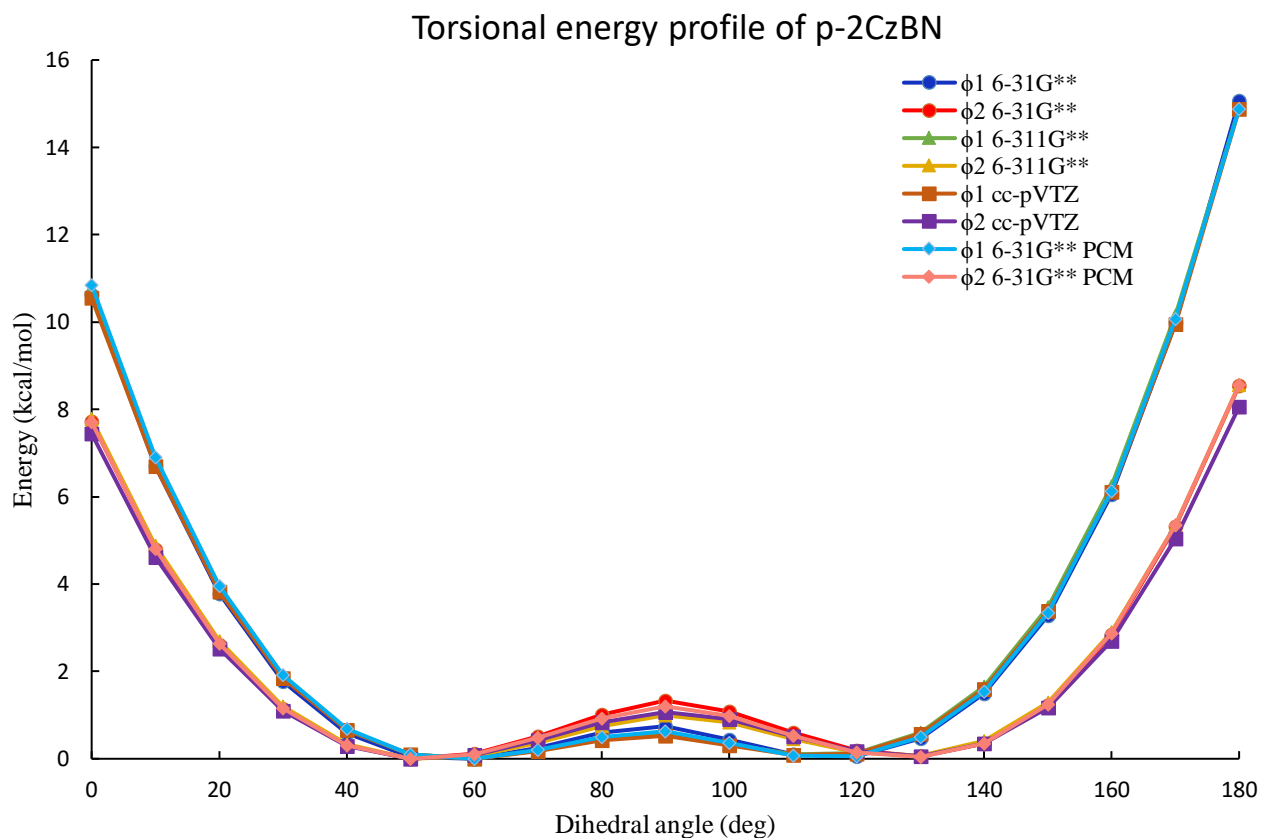
Figure 3.4.1 Comparison of torsional potential energy profile of p-2CzBN through the dihedral angles φ_1 and φ_2 with the level of calculation PBE1PBE/6-31G**, PBE1PBE/6-311G** and PBE1PBE/cc-pVTZ.
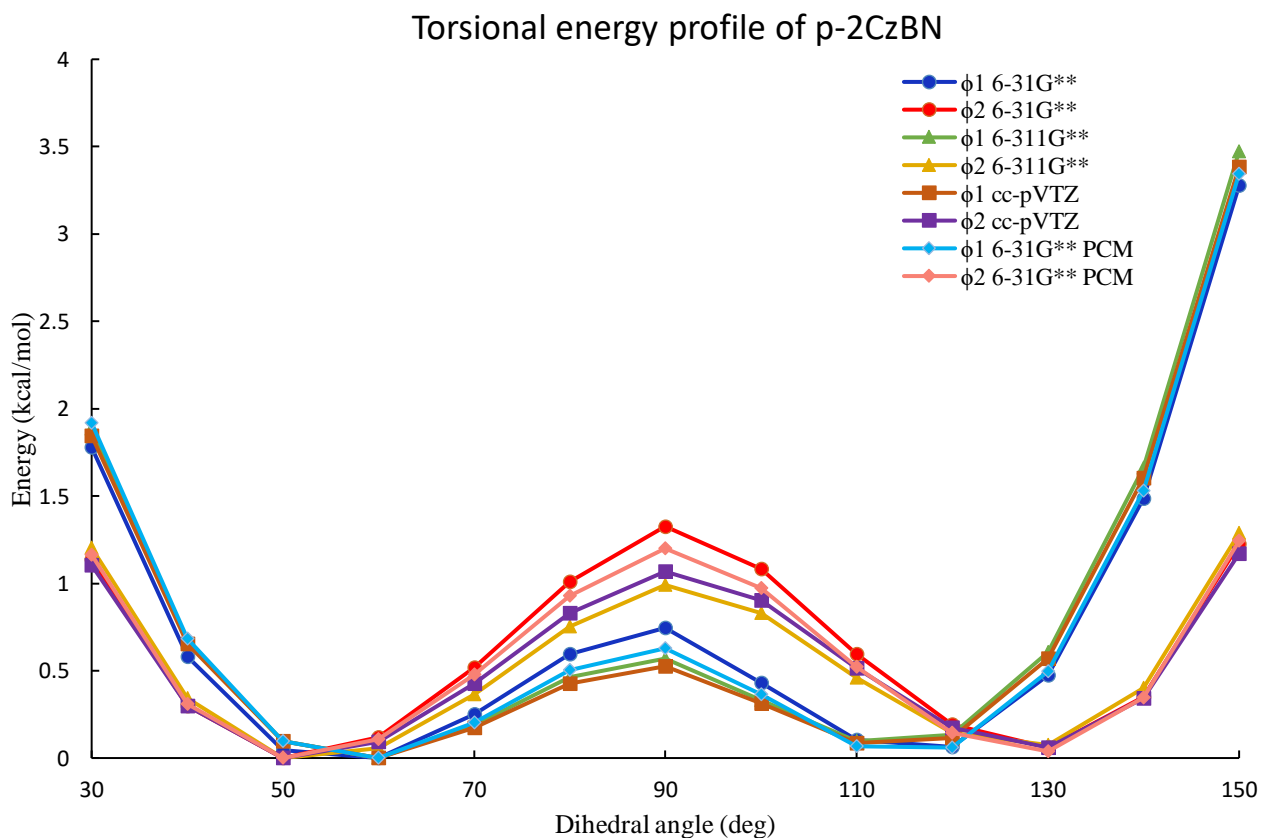

Figure 3.4.2 Zoom of figure 3.4.1.

The potential energy scan of each dihedral angle of 5CzBN was also computed with PBE1PBE/6-31G** level. We computed the PES scanning only two dihedral angles, φ_1 and φ_4, as the molecule is symmetric with respect to the plane perpendicular to the benzonitrile ring and passing through the CN bond. Also, in this case the dihedral angles were scanned from 30° to 150° both φ_1 and φ_4. The profiles are shown in figure 3.4.3.

Also for 5CzBN the torsional energy profiles of both dihedral angles are similar, even more that for p-2CzBN. The two minima points are also found at $\pm 60^o$ and $\pm 120^o$ as for φ_2 of p-2CzBN. The saddle point is at the dihedral angle equal to $\pm 90^o$ with a difference in energy with respect to the minima points of 2.4 kcal/mol, while for p-2CzBN the difference in energy with respect to the minima points is 0.6 kcal/mol..
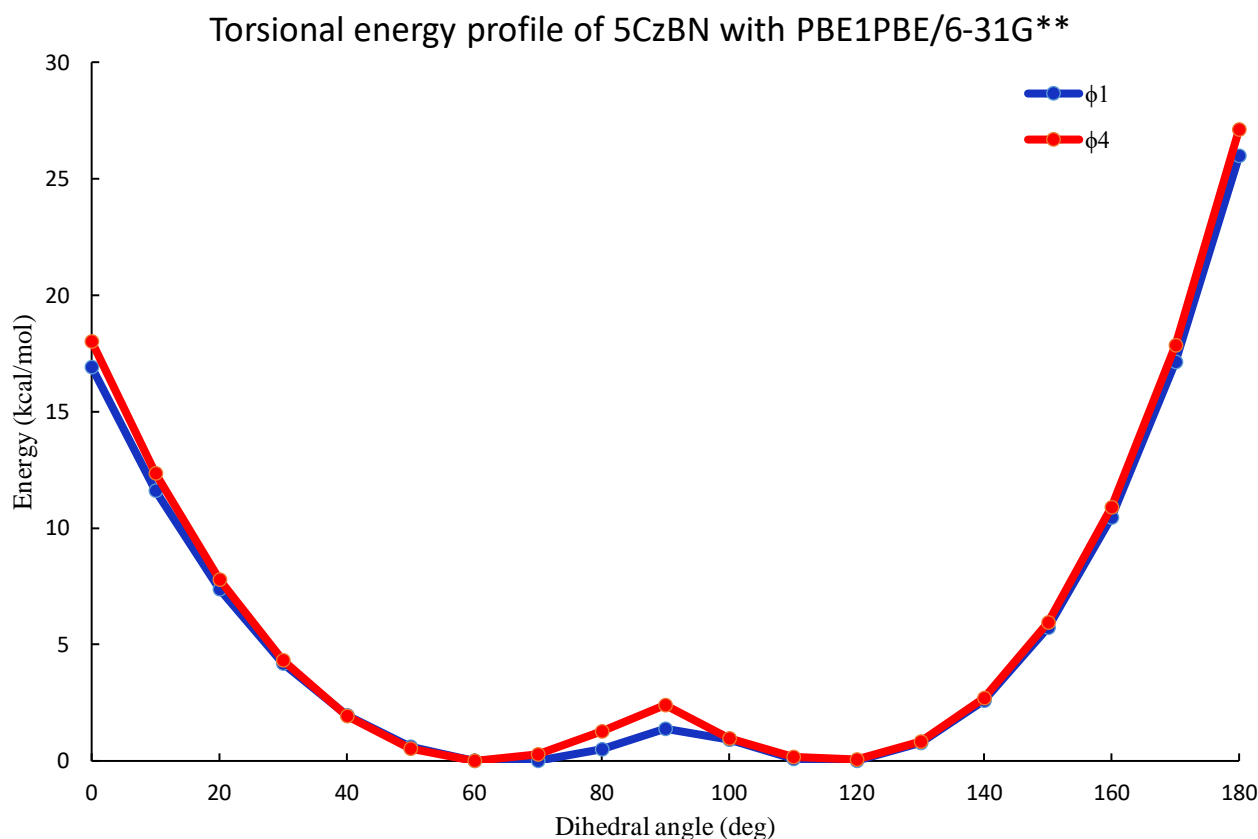

Figure 3.4.3 The potential energy surface relaxed scan of 5CzBN through the dihedral angles φ_1 and φ_4 with the level of calculation PBE1PBE/6-31G**.

We also compare the potential energy scan of p-2CzBN and 5CzBN with the same level of calculation PBE0/6-31G*. As it can been seen in figure 3.4.4, the relative energies of the two molecules have a different profile: when steric repulsion is increasing, the relative energy of and 5CzBN is higher than that of p-2CzBN at the same dihedral angle.
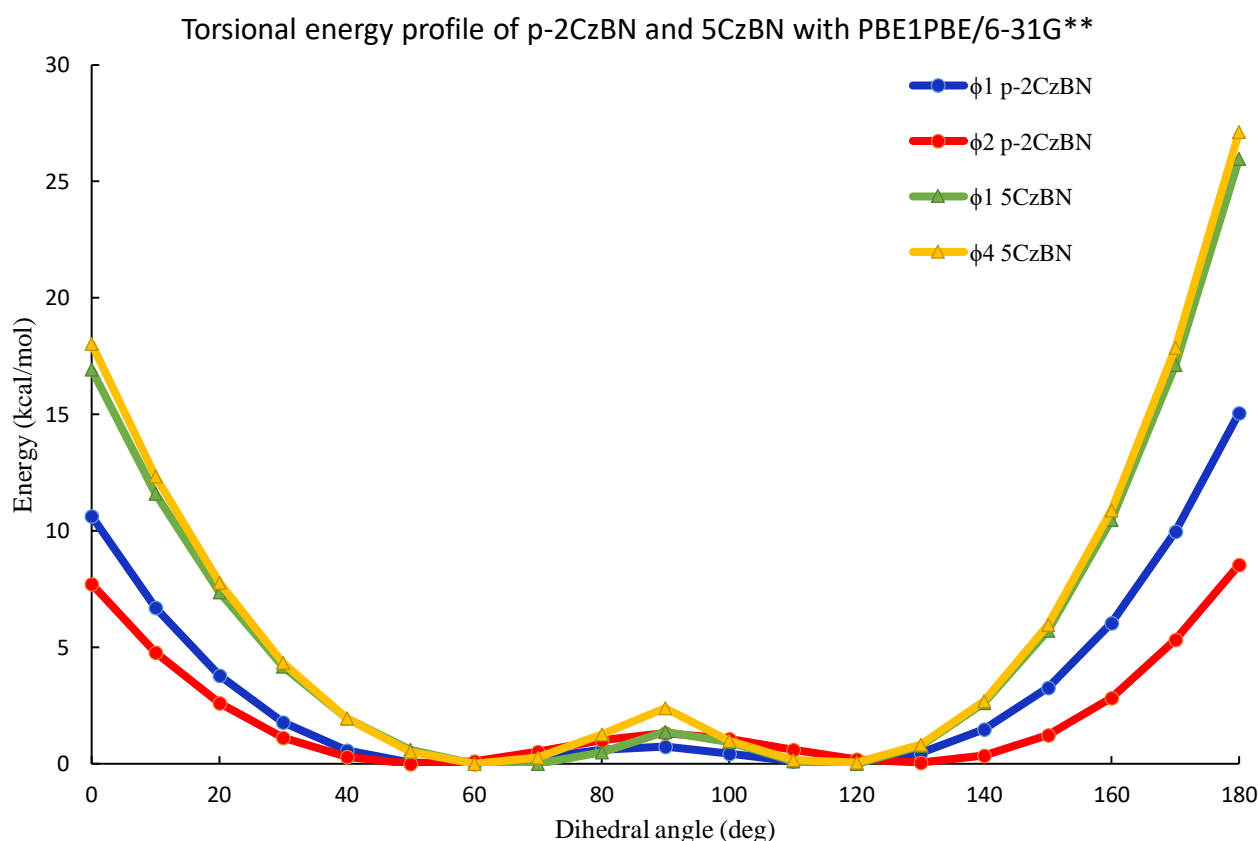
Figure 3.4.4 Comparing the torsional energy profile between p-2CzBN and 5CzBN with the level of calculation PBE1PBE/6-31G**.

The optimized conformations of the first excited state and triplet state are also computed. We started with the optimized first singlet excited state (S_1) of p-2CzBN with TDA-PBE1PBE/6-31G** level of calculation. The S_1 potential energy surface of p-2CzBN was computed keeping fixed one dihedral angle φ_1 while letting the other one relax φ_2 and vice versa. The dihedral angle was scanned from 0° to 180° like for the S_0 profile. The T_1 potential energy surface scan was computed with TDA-PBE1PBE/6-31G**. The potential energy profile of S_1 and T_1 are shown in figure 3.4.5 for φ_1 and in figure 3.4.6 for φ_2 where the Franck-Condon point of $S_0 \rightarrow S_1$ is $\pm 90^o$ for φ_1 and $\pm 50°$, $\pm 130°$ for φ_2. The carbazole ring is rotating when its ring is almost perpendicular to benzonitrile ring, leading the lower energy in S_1 state for φ_1. While for φ_2 the lower energy in S_1 state is equal to the state S_0. On the other hand, the T_1 energy profile is similar to S_0 energy profile where the Franck-Condon points of $S_0 \rightarrow T_1$ are located at $\pm 60^o$, $\pm 120^o$ for φ_1 and $\pm 50°$, $\pm 130°$ for φ_2.
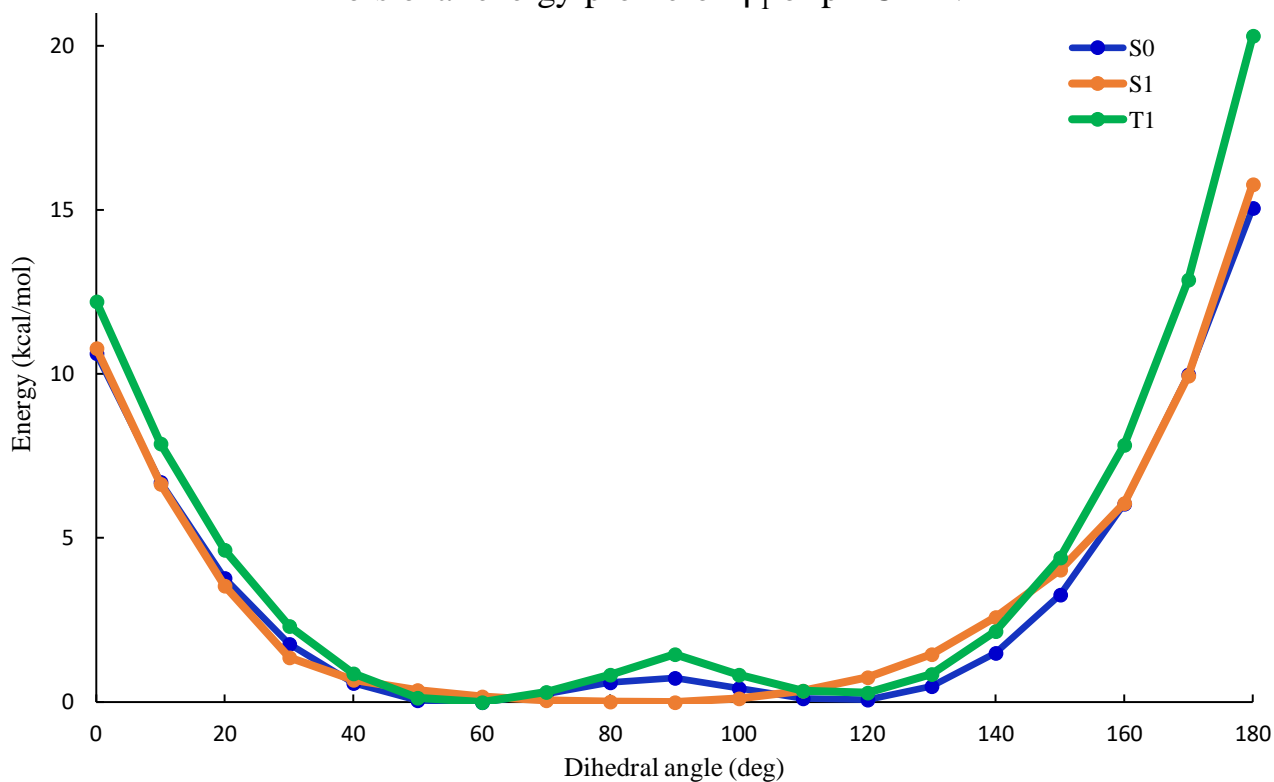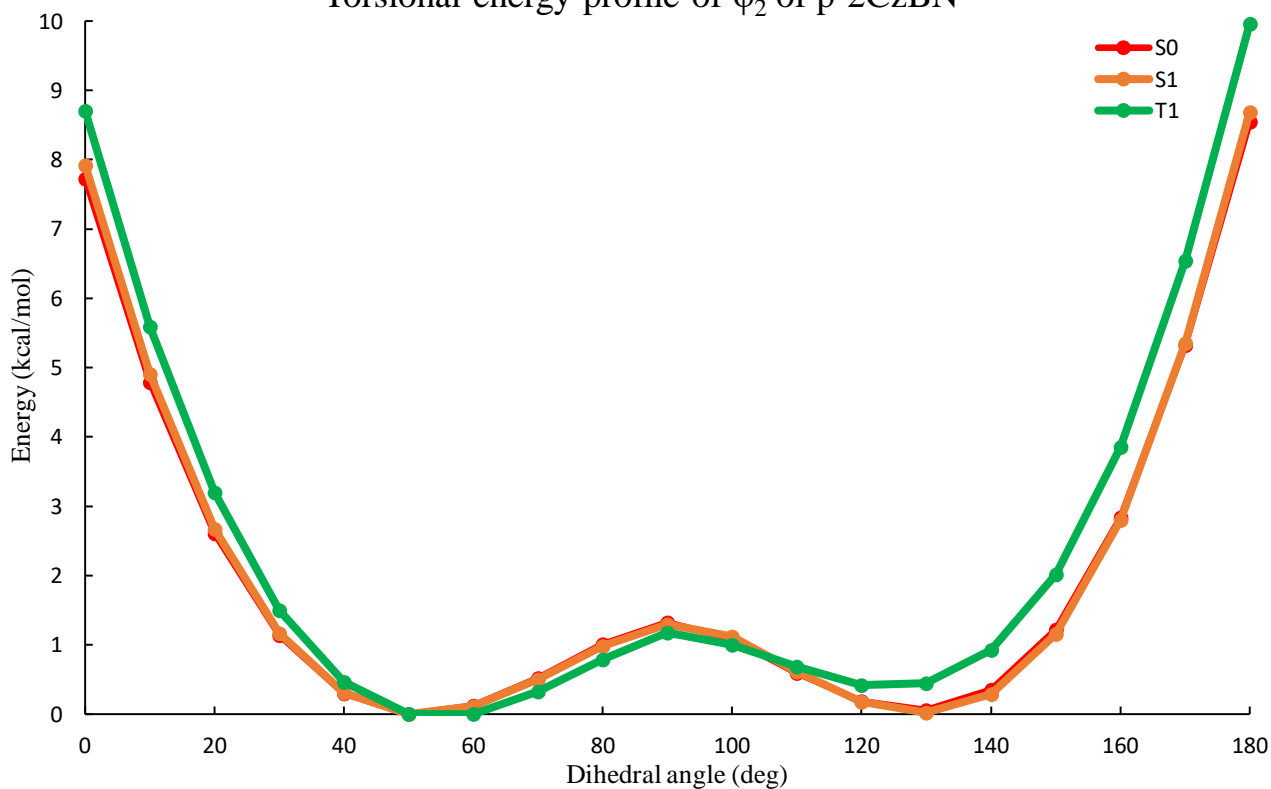
Figure 3.4.5 Comparison of the PES profiles of φ_1 of 2CzBN for S_0, S_1 and T_1 optimized geometries with the level of calculation PBE1PBE/6-31G** and TDA-PBE1PBE/6-31G** respectively.

Figure 3.4.6 Comparison of the PES profiles of φ_2 of 2CzBN for S_0, S_1 and T_1 optimized geometries with the level of calculation PBE1PBE/6-31G** and TDA-PBE1PBE/6-31G** respectively.

3.5 Mapping of calculated state energies and oscillator strengths

The conformation of p-2CzBN and 5CzBN was then mapped through DFT calculations carried out fixing both dihedral angles (φ_1 and φ_2), to calculate state energies and oscillator strengths at different conformations. The calculation was performed with PBE1PBE/6-31G**. The potential energy scan map of the ground state was scanned from ±30° to ±150° degree while fixing both dihedral angles. The results are shown in figures 3.5.1 (for p-2CzBN) and 3.5.2 (for 5CzBN), where four global minima appear at both dihedral angles of ~ ±60°- ±50° and ±120°- ±130° for p-2CzBN and two global minima appear at both dihedral angles of ~ ±60° and ±120° for 5CzBN. These global minima conformers can be thermally accessible one from another due to the relatively low energy at the saddle point on the map ($\varphi_1 = \pm90^\circ$ and $\varphi_2 = \pm90^\circ$), for which the energy barrier is approximately 2.5 kcal/mol either in p-2CzBN and 5 kcal/mol in 5CzBN.
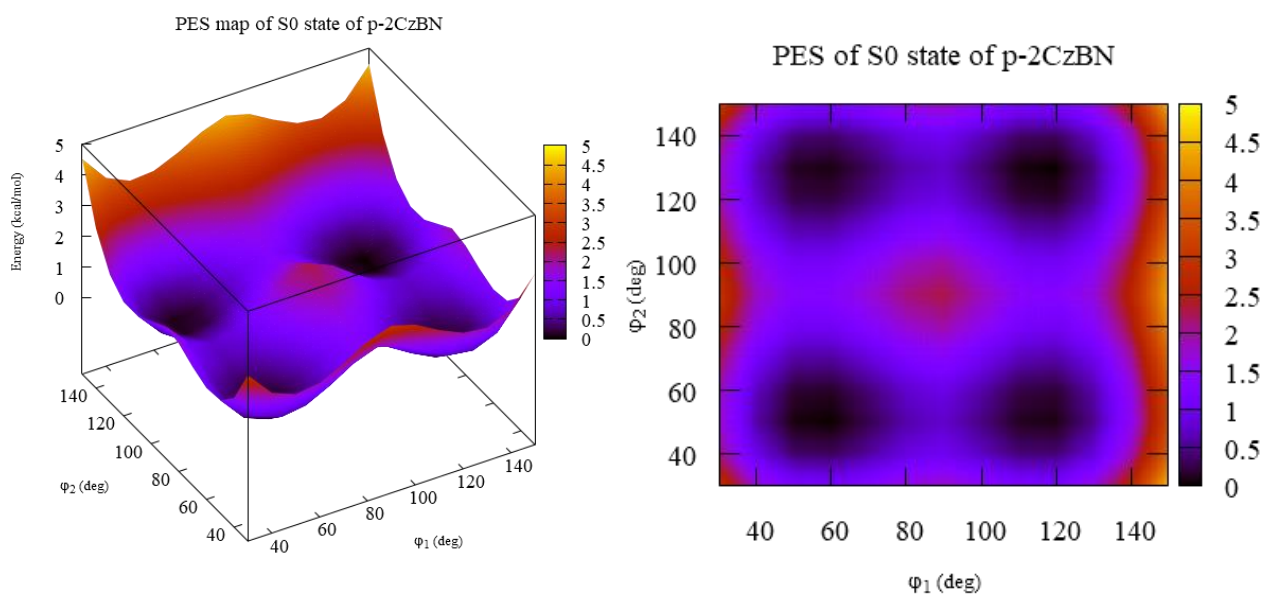

Figure 3.5.1 The potential energy surface scan (kcal/mol) of p-2CzBN through the fixed dihedral angles φ_1 and φ_2 with PBE1PBE/6-31G** (left) side view (right) top view.
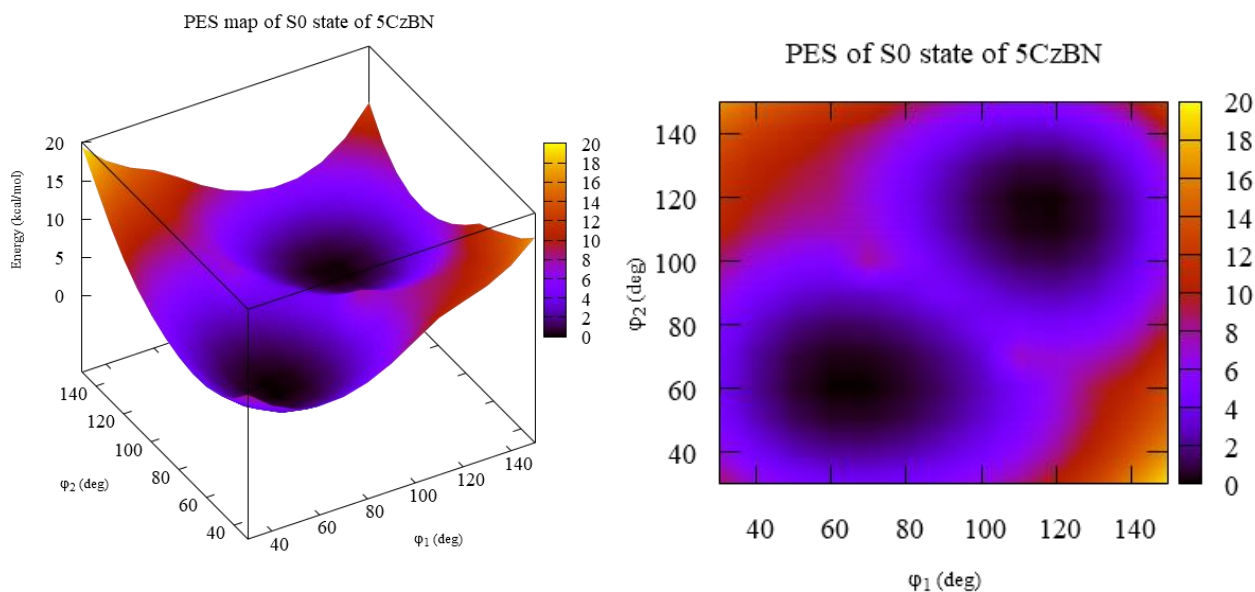
Figure 3.5.2 The potential energy surface scan (kcal/mol) of 5CzBN through the fixed dihedral angles φ_1 and φ_4 with PBE1PBE/6-31G** (left) side view (right) top view.

The TDA-DFT potential energy maps of excited states were also computed with single point TDA-PBE1PBE/6-31G** calculations carried out at the optimized ground states geometries. The map of vertical energy gap between S_1 and T_1 state are computed and the ΔE^{ST} map of p-2CzBN and 5CzBN are given in figure 3.5.3. The lower region of ΔE^{ST} is located at the middle of the map when carbazole ring is almost perpendicular to benzonitrile ring. Therefore, the lower region of ΔE^{ST} is not close to the Franck-Condon points, but it can be thermally accessible, since the PES of T_1 state in figure 3.5.4 shows that this region is a saddle point with an energy barrier of 3 kcal/mol. While for 5CzBN the lower region of ΔE^{ST} is located almost at the Franck-Condon points of the map. Therefore, in this case the lower region of ΔE^{ST} it can be thermally accessible.
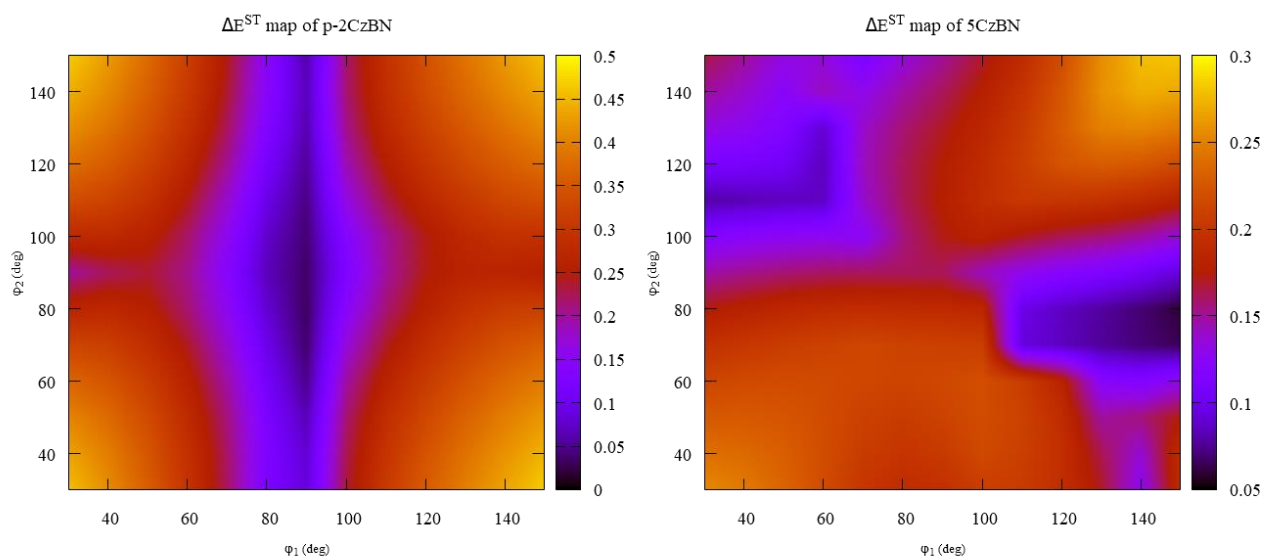
Figure 3.5.3. The ΔE^{ST} (eV) at PBE1PBE/6-31G** level p-2CzBN (left) 5CzBN (right) calculated at the ground state geometry.

The potential energy map of S_1 and T_1 excited state at the optimized ground state geometries, are shown respectively in figure 3.5.4 and 3.5.5. For p-2CzBN: the lowest energy of S_1 state is achieved when one carbazole ring are almost perpendicular with respect to the benzonitrile and the other is at ±50° and ±130°. Moiety on the other hand, the PES of T_1 is similar to the potential energy profile of the optimized ground state (shown in figure 3.5.1). The highest energy in S_1 and T_1 occurs when the steric strain of both carbazole rings is maximum. The lower region of ΔE^{ST} is located in between the two Franck-Condon points, precisely at the saddle point in optimized ground state map. Reaching on T_1 the region of lower vertical ΔE^{ST} is thermally possible, since the difference between the lowest energy and saddle point in T_1 is approximately 3 kcal/mol. While for 5CzBN: the lowest energy of S1 state is achieved when both carbazole ring are at ±60° with respect to the benzonitrile. In this case a scan from ±30° to ±100° was carried out; the highest energy in S1 occurs when the steric strain of both carbazole rings is maximum.

Figure 3.5.4. The potential energy of excited state (kcal/mol) of p-2CzBN at PBE1PBE/6-31G** level with respect to optimized ground state geometries: energy map of first singlet state (left) and energy map of first triplet state (right) calculated at the ground state geometry.
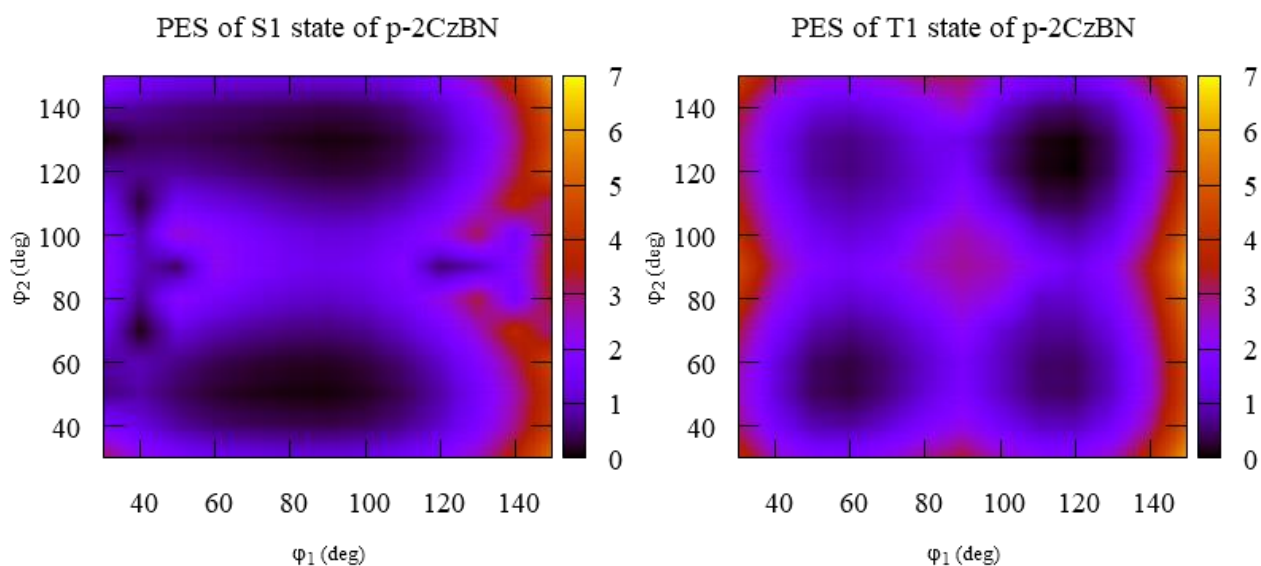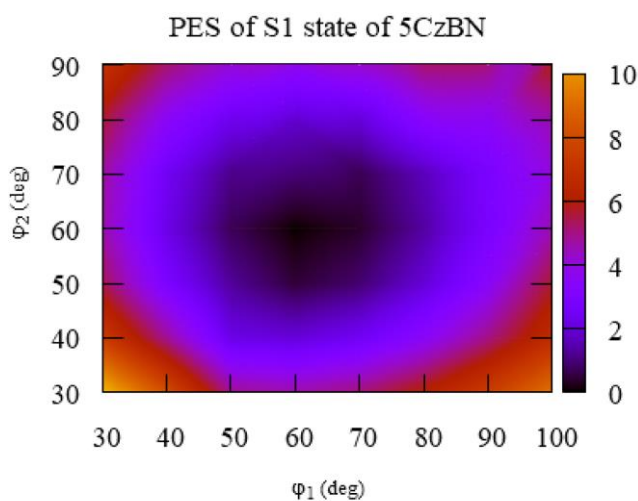

Figure 3.5.5. The potential energy of excited state (kcal/mol) of 5CzBN at PBE1PBE/6-31G** level with respect to optimized ground state geometries: energy map of first singlet state calculated at the ground state geometry.

As we are mainly interested in the emission from the first excited state to the ground state, the corresponding oscillator strength (O.S.) map of p-2CzBN and 5CzBN was also constructed. In figure 3.5.6, the O.S. of $S_0 \rightarrow S_1$ is very low only at the points corresponding to ±90° for both molecules. For 5CzBN the O.S. is a little lower than for p-2CzBN. The problem of low oscillator strength arises from the small spatial overlap between the HOMO and LUMO, leading to suppression of the oscillator strength. when the dihedrals angles become planar there is more conjugation, therefore HOMO and LUMO are more delocalized, while near 90 ° the opposite occurs.
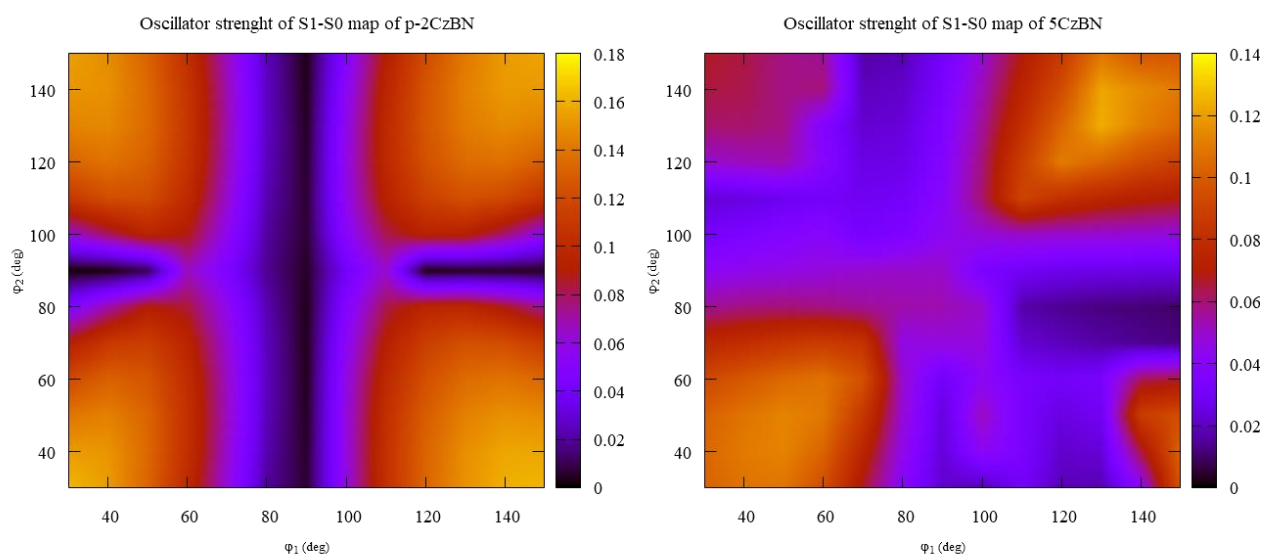
Figure 3.5.6 The oscillator strength map of first excited singlet state (S$_1$) of p-2CzBN (left) and 5CzBN (right).

Considering the results of PES maps, ΔE^{ST} maps and oscillator strength (O.S) maps. In order for TADF to take place, the most accessible area for both molecules is the one between dihedral angles from ±60 ° to ±90 ° and ±90 ° - ±120 °.

Chapter 4

Characterization of the nature of excited states and of their crossing

To understand the efficiency of the TADF process, it is very useful to characterize the nature of excited states which are involved in. To this end, the development of metrics based on charge density is particularly suitable to quickly classify the charge transfer (CT) or locally excited (LE) character of a transition. To this end, the spatial separation of the frontier orbitals was characterized by a metric based on the hole and electron distance (Δr, equation 4.3). Also, the overlap ϕ_S between the attachment and detachment density matrices was calculated by using equation 4.2. The two parameters are calculated by using the MESRA software.

The detachment and attachment density matrices are given by Γ and Λ[31]. For a given electronic transition between two states, it is possible to define two three dimensional function ϱ_τ and ϱ_A representative of the spatial distribution of the electronic density removed (detachment) from the initial state and reorganized (attachment) in the final one during the transition (figure 4.1)[31].

The integration of charge density of detachment (ϱ_τ) or attachment (ϱ_Λ) through the three-dimensional space gives the total charge (the number of electrons) ϑ_τ involved in the transition, typically one:

$$\vartheta_\tau = \int_R d\xi_1 \int_R d\xi_2 \int_R d\xi_3 \varrho_\tau(\xi_1\xi_2\xi_3) \equiv \int_{R^3} d^3\xi \varrho_\tau(\xi) \qquad (4.1)$$
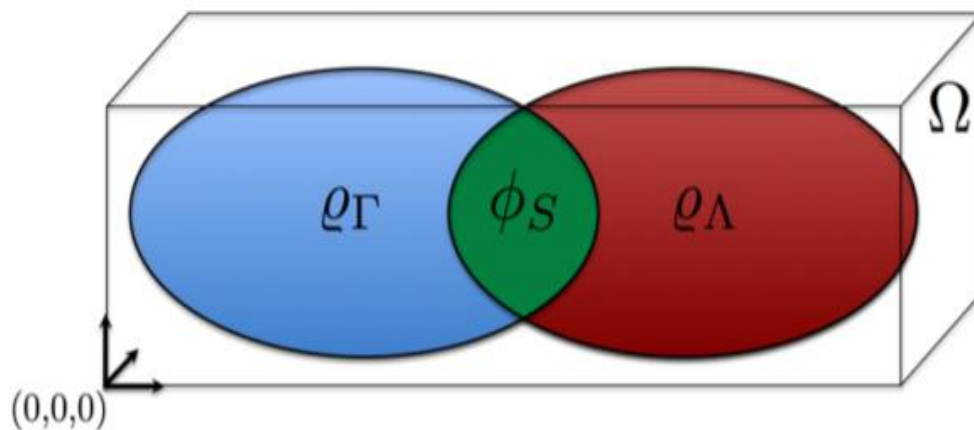
$$\tau \equiv \Gamma, \Lambda$$

Figure 4.1 Graphical depiction of the ϕ_S descriptor as the overlap between detachment and attachment densities. Figure adapted from reference 32.

A dimensionless parameter ϕ_S can be then defined as the overlap between the attachment and detachment densities. Following equation 4.2, the ϕ_S index can range from 0 to 1, depending on the strength CT character of the electronic transition (0: full CT, 1: no CT).

$$\phi_S = \vartheta^{-1} \int_{R^3} d^3\xi \sqrt{\varrho_\Gamma(\xi)\varrho_\Lambda(\xi)} \tag{4.2}$$

$$\phi_S \in [0:1]$$

Where ϑ is the average charge contained in the attachment and detachment charge density functions. The product $\varrho_\Gamma(\xi)\varrho_\Lambda(\xi)$ will be different from zero only in the regions in which there is overlap between the two charge distributions (green region in figure 4.1), so that the highest values of ϕ_S are obtained when the transition results in a zero photoinduced electronic density change (LE), while low values indicate that there is no overlap between detachment and attachment densities (CT transition)[32]. Therefore, ϕ_S quantitatively represents the charge separation nature of a chromophore upon light absorption.

It can be interesting to quantitively provide the coefficient-weighted hole-electron distance (Δr) between a set of orbital centroids. The hole−electron pair interactions could be related to the distance covered during the excitations, so it can be calculated by following equation.

$$\Delta r = \frac{\sum_{ia} K_{ia}^2 |\langle\varphi_a|r|\varphi_a\rangle - \langle\varphi_i|r|\varphi_i\rangle|}{\sum_{ia} K_{ia}^2} \tag{4.3}$$

Where $K_{ia} = X_{ia} + Y_{ia}$ (X_{ia} and Y_{ia} are excitation and de-excitation coefficients produced by the TDA-DFT calculation), $\langle\varphi_i|r|\varphi_i\rangle$ is the norm of an occupied orbital centroid and $\langle\varphi_a|r|\varphi_a\rangle$ is the norm of virtual orbital centroid[33]. Also, through the value of Δr it can be quantified the nature of an excited state either with charge transfer ($\Delta r \geq 2.0\ A°$) or local excitation ($\Delta r \leq 2.0\ A°$)

character. However, if two acceptors are disposed (nearly) symmetrically around a single donor (e.g. in the case of 5CzBN), even a long-range charge-transfer transition can result in $\Delta r \approx 0$, a disadvantage which makes the metric ϕ_S superior to Δr.

Prior to the calculation of the metrics, the reorganization of the electron density upon electronic transition to the excited states at the ground state geometry was analyzed through the visualization of the attachment and detachment densities. For the transition from the S_0 state to S_1, p-2CzBN and 5CzBN qualitatively show a CT character (detachment and attachment densities localized in different part of the molecule) in figure 4.2 (top) and 4.3 (top), while the S_0 to T_1 transition shows a high LE character, figure 4.2 (bottom) and 4.3 (bottom). The S_0-S_2 transition also exhibit a CT character as the one to the S_1 state. Interestingly, the T_2 state of p-2CzBN shows a mixed character, in between CT and LE, while T_2 state of 5CzBN shows a pure CT character (figure 4.4), at least judging from the qualitative visualization criterion.
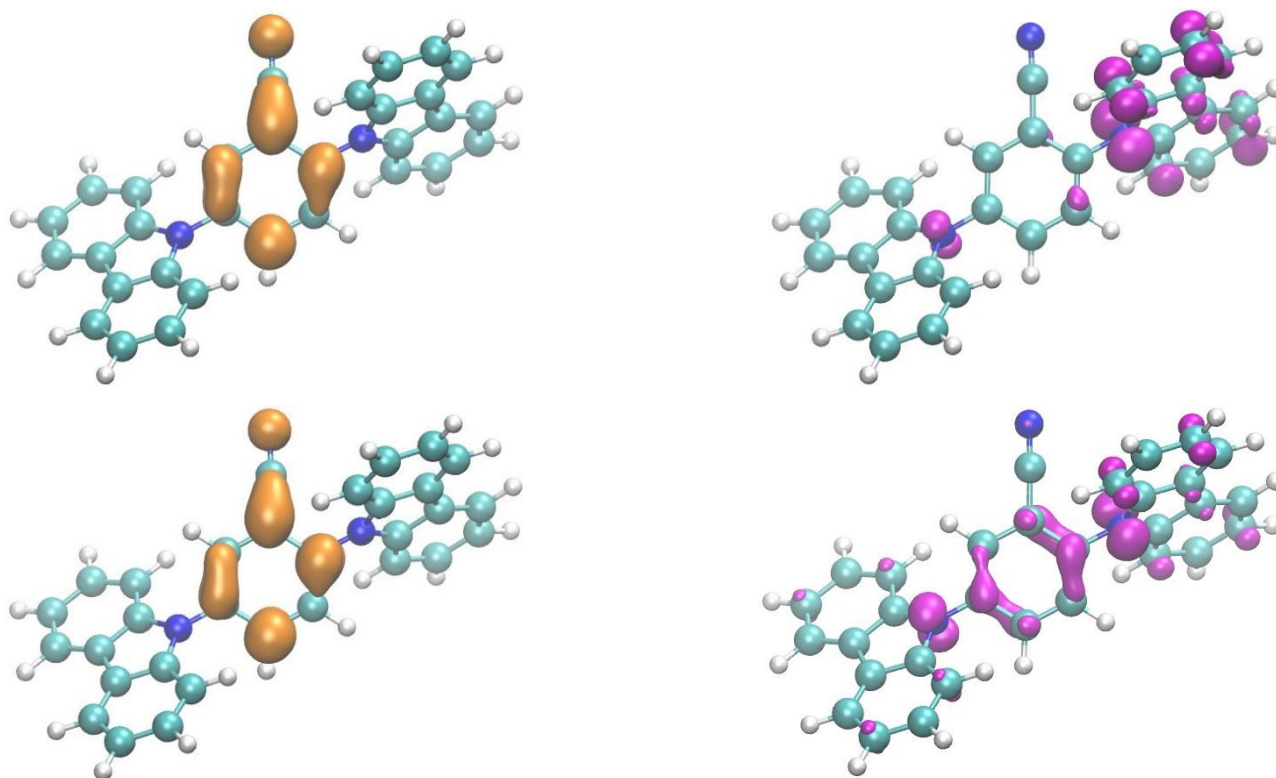

Figure 4.2 Electron (attachment orange isocontour) and hole (detachment magenta isocontour) densities of p-2CzBN obtained in the attachment/detachment formalism from TDA-PBE1PBE/6-31G** calculations ($\varphi_1 = 60°$, $\varphi_2 = 50°$) S_0-S_1 transition (top) and S_0-T_1 transition (bottom).
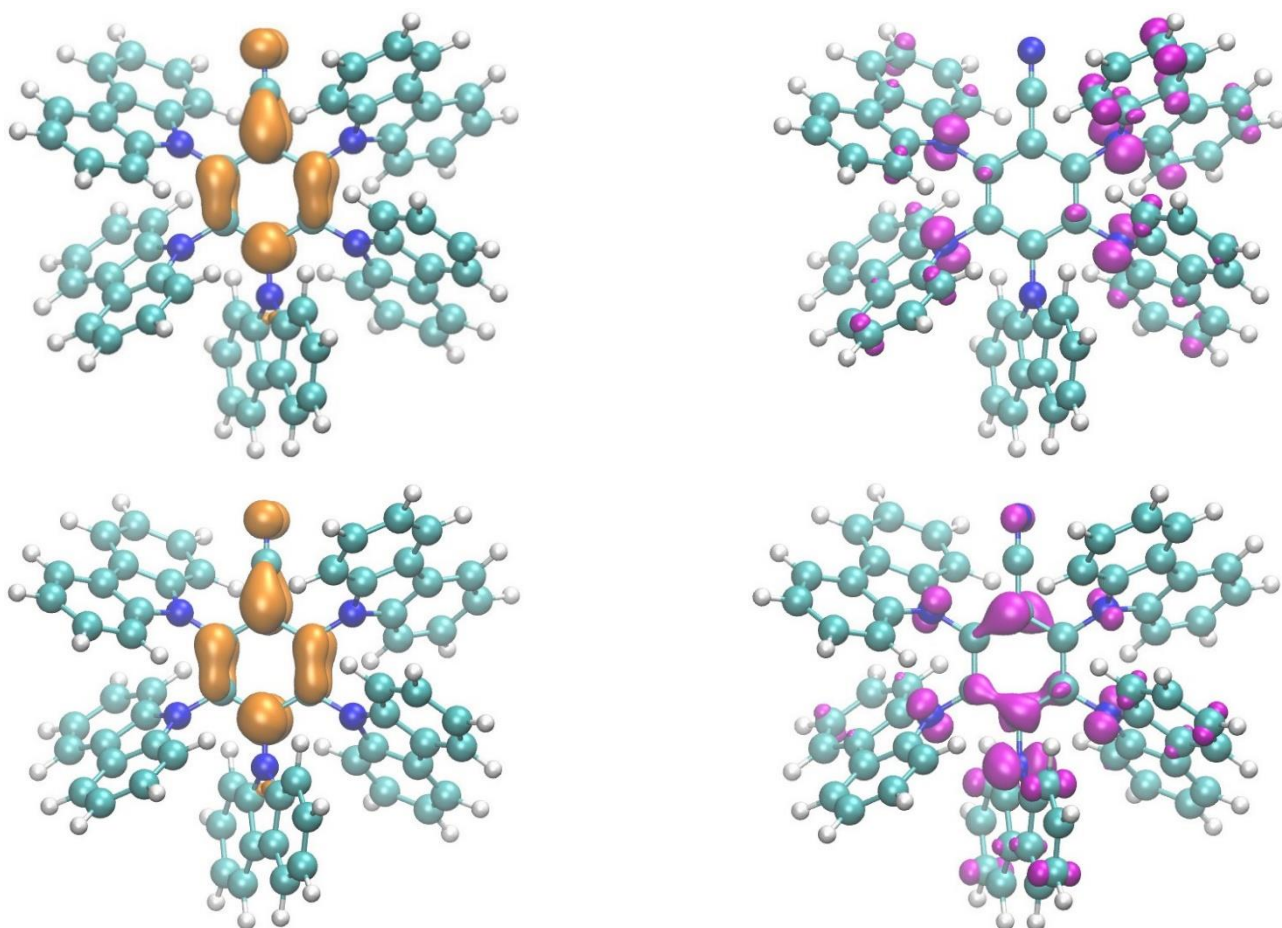
Figure 4.3 Electron (attachment orange isocontour) and hole (detachment magenta isocontour) densities of 5CzBN obtained in the attachment/detachment formalism from TDA-PBE1PBE/6-31G** calculations ($\varphi_1 = 60°$, $\varphi_2 = 60°$) S_0-S_1 transition (top) and S_0-T_1 transition (bottom).
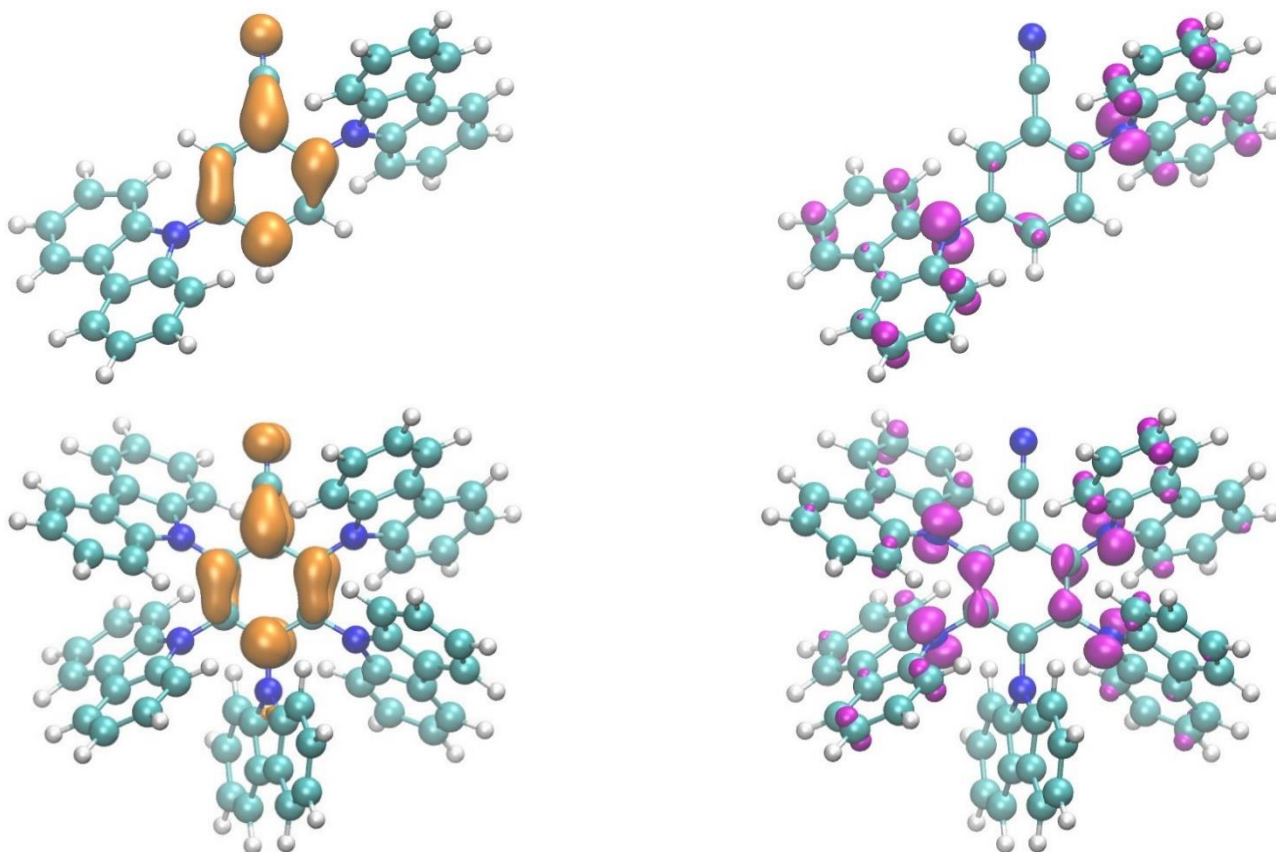
Figure 4.4 Electron (attachment orange isocontour) and hole (detachment magenta isocontour) densities from S_0 to T_2 obtained in the attachment/detachment formalism from TDA-PBE1PBE/6-31G** calculations ($\varphi_1 = 60°$, $\varphi_2 = 50°$ for p-2CzBN (top) and $\varphi_1 = 60°$, $\varphi_2 = 60°$ for 5CzBN (bottom).

We also quantitively characterized the nature of excited states by defining CT(LE) character with Δr largely above 2.0 Å (close to 0 Å) and ϕ$_s$ close to 0 (1). The values reported in table 4.1 confirm for both molecules, that S_1 and S_2 exhibit a CT character, while T_1 shows the strong a LE character. It can be noticed that Δr of 5CzBN does not follow the criterion that $\Delta r \geq 2.0$ Å for charge transfer character and $\Delta r \leq 2.0$ Å for locally excitation character. This is because of the symmetric D-A-D architecture, when the hole and electron distance are calculated by orbital centroid. In fact, as the D-A-D structure has a symmetry between A unit, consequently, even though the hole density is localized on carbazoles and the electron one on the benzonitrile, their centroids are very close or coincident. Therefore, Δr cannot be used to quantify the nature of excited state for D-A-D system. We also noticed that for 5CzBN the energy of T_2 state is close to that of T_1 state (approximately 0.05 eV), and lower than the S_1 energy, therefore also T_2 could play a role in the TADF process. However, this does not hold for T_2 in p-2CzBN, and this could be one of the reasons why 5CzBN is a TADF active emitter and p-2CzBN could be not.

Table 4.1 Excited state characterization of p-2CzBN ($\varphi_1 = 60^\circ$, $\varphi_2 = 50^\circ$) of 5CzBN ($\varphi_1 = 60^\circ$, $\varphi_4 = 60^\circ$) where the values of ϕ_S, Δr and nature of the electronic transition from the ground state are shown in the table. Note that the oscillator strength is only defined for singlet excitation.

	State	E (eV)	O.S	ϕ_S	Δr (Å)	CT/LE
	S_1	3.2859	0.1043	0.3687	2.3059	CT
	S_2	3.5763	0.0094	0.3452	2.8769	CT
p-2CzBN	T_1	3.0082	-	0.6074	0.6481	LE
	T_2	3.3955	-	0.4858	0.6374	CT/LE
	S_1	2.9568	0.1070	0.4070	0.7179	CT
	S_2	2.9895	0.0478	0.3407	0.6199	CT
5CzBN	T_1	2.7410	-	0.6447	1.6591	LE
	T_2	2.7922	-	0.4531	0.4261	CT

We also calculated the ϕ_S maps of excited states at other geometries in order to determine the variation of excited state nature with respect to possible conformational changes induced by temperature. These calculations, reported in figure 4.5, confirm that S_1 and S_2 of p-2CzBN exhibit a CT character, and T_1 exhibits a LE character, while T_2 shows a mixed character, in fact, for φ_1 and φ_2 between $\pm 60^\circ$ and $\pm 100^\circ$ it is CT-like, while for all the other dihedral angles it shows LE character.
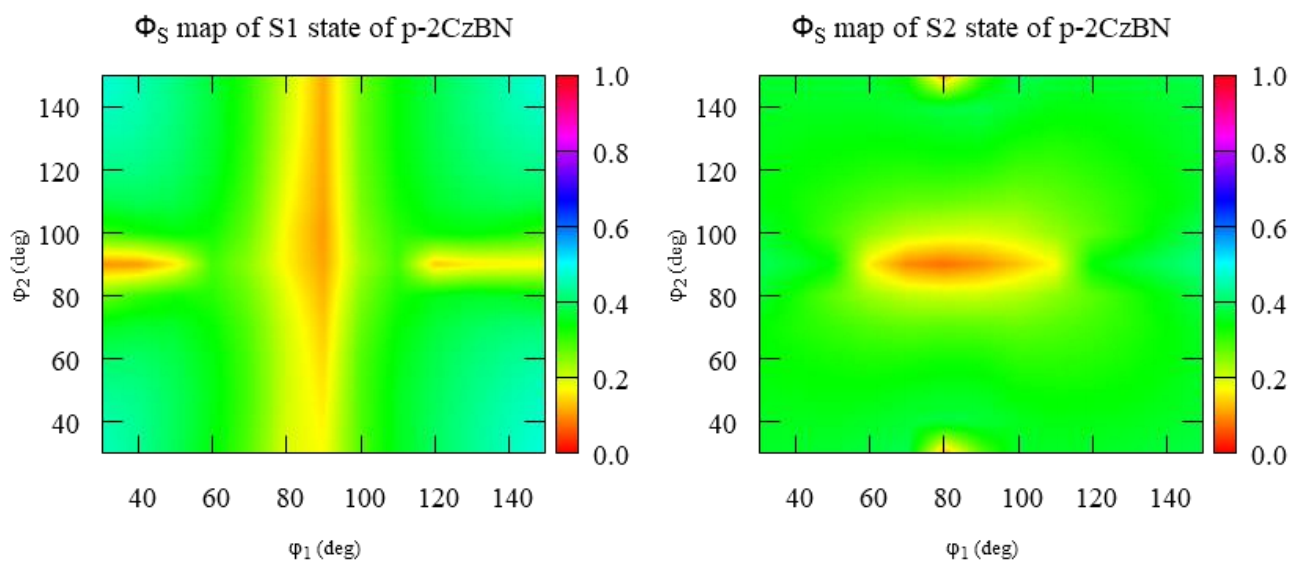
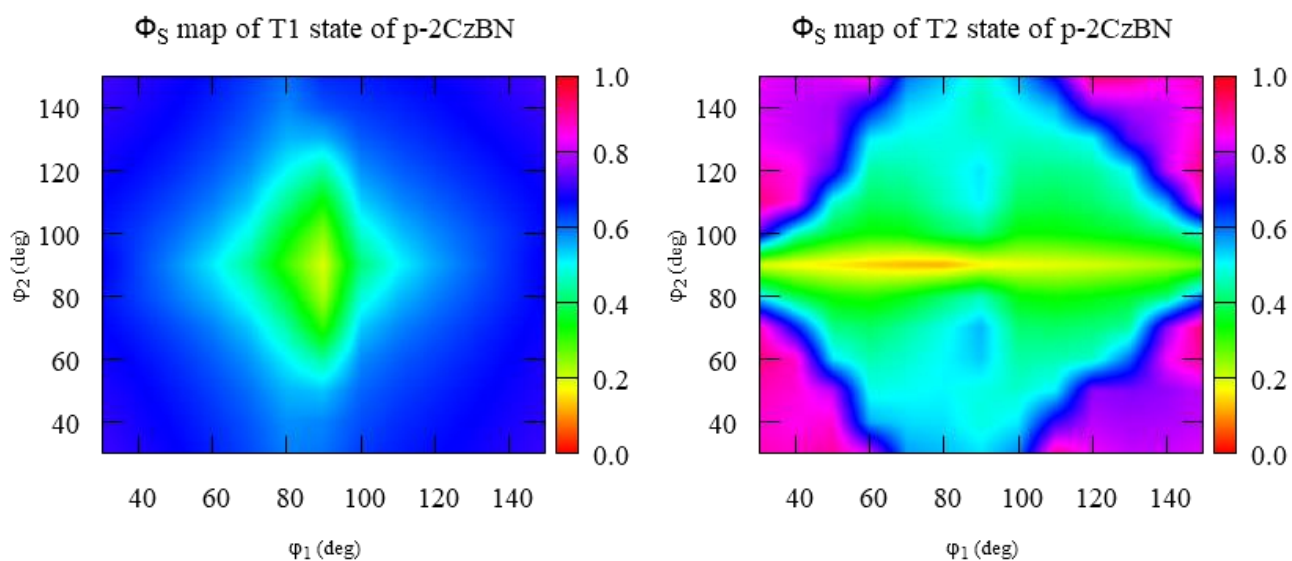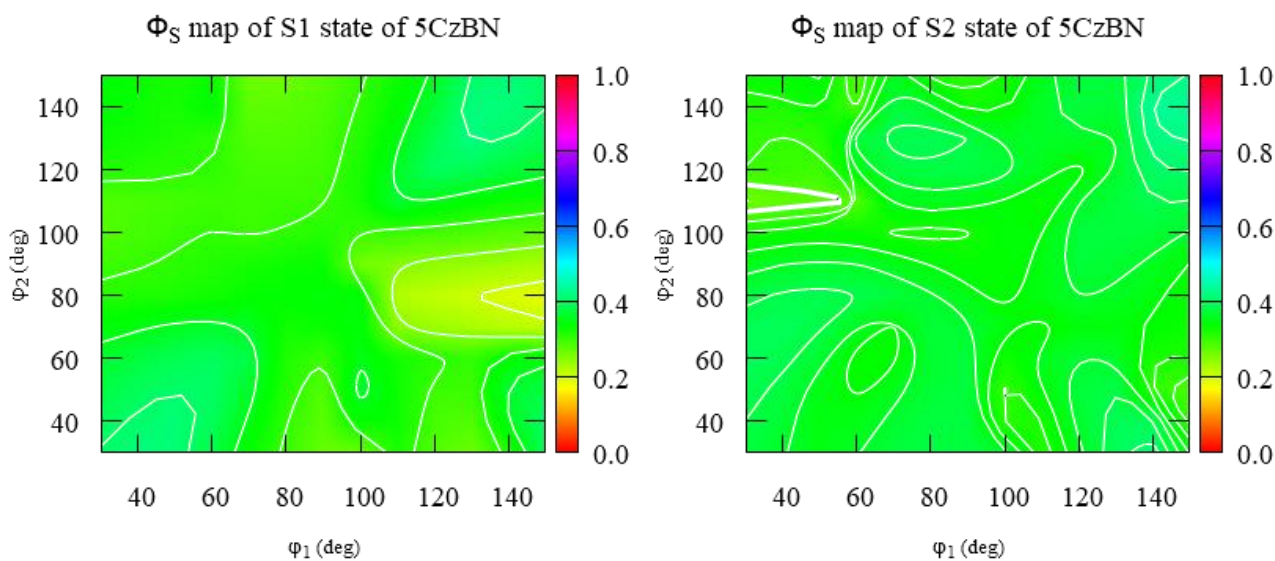**Figure 4.5** ϕ_S map of p-2CzBN, S_0-S_1 transition (top left), S_0-S_2 transition (top right), S_0-T_1 transition (lower left) and S_0-T_2 transition (lower right).

For 5CzBN (figure 4.6), the ϕ_S map shows that S_1 and S_2 states still exhibit a CT character, but less than for the p-2CzBN molecule. On the other hand, the T_1 state shows LE character as in p-2CzBN. Interestingly, T_2 state exhibits a character CT unlike p-2CzBN. More in general, the nature of the states of p-2CzBN is robust with respect to conformational changes, while for 5CzBN the variations of the nature of singlet states are a bit larger, even if not dramatic.
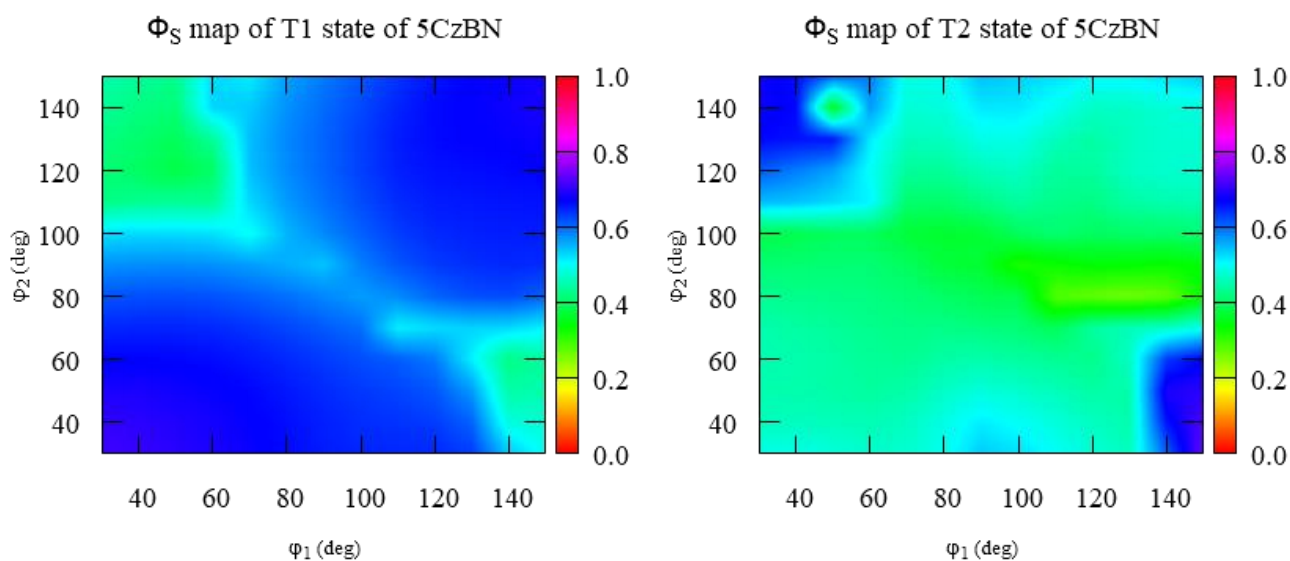
Figure 4.6 ϕ_S map of 5CzBN S_0-S_1 transition (top left), S_0-S_2 transition (top right), S_0-T_1 transition (lower left) and S_0-T_2 transition (lower right).

In the chapter 2, we described how the rate of RISC does not only depend on ΔE^{ST}, but also on the spin-orbit coupling between the involved singlet and triplet states. Therefore, we also calculated the spin-orbit coupling between S_1 and T_1 state using Fermi's golden rule without considering the coupling between electronic and vibrational motion. The spin-orbit coupling elements were calculated using the Breit-Pauli spin-orbit Hamiltonian with effective charge approximation, as implemented in the software ORCA. The latter, in turn, takes as input the wave function files produced by Gaussian TDA-DFT calculations. The result is shown in figure 4.7. As it can be seen in the maps, SOC between S_1 and T_1 state of 5CzBN is a bit higher than for p-2CzBN, another hint towards a more effective TADF process for the former molecule.
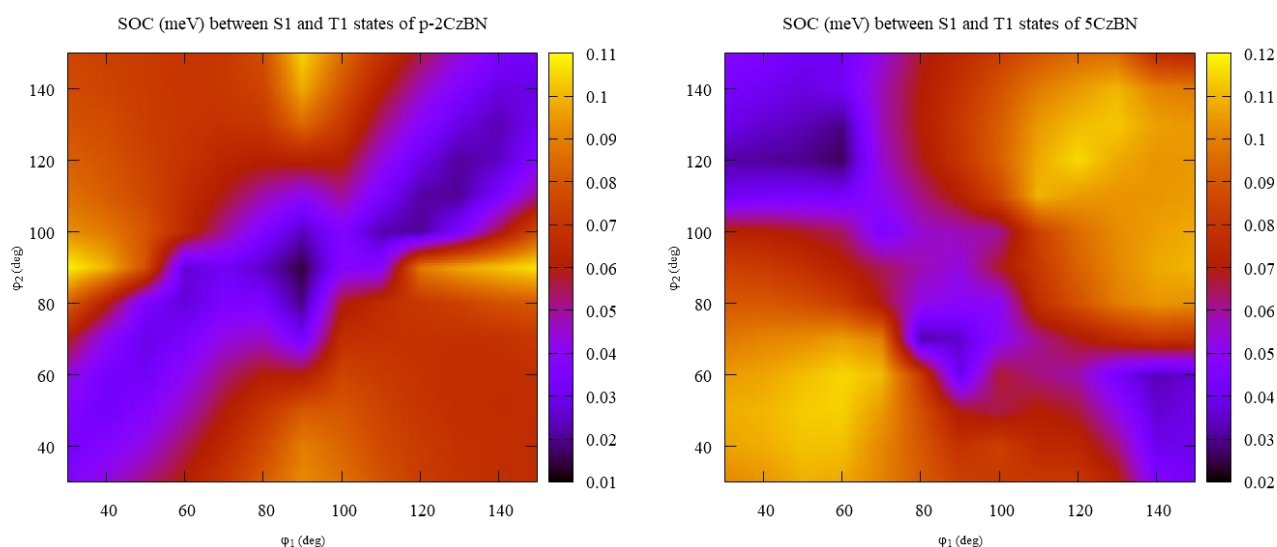
Figure 4.7 Spin-orbit coupling constant (meV) map between S_1 and T_1 states of p-2CzBN (left) and 5CzBN (right) with TDA-PBE1PBE/6-31G**.

As we mentioned above, the closeness in energy between T_1 and T_2 states, and also the fact that T_2 is lying lower than S_1 state, may play an important role in carbazole-benzonitrile system for TADF performance. To support this possibility, the spin-orbit coupling between S_1 and T_2 state was also computed and shown in figure 4.8. As we can see, 5CzBN has lower value for spin-orbit coupling in some region on the map, as well as the spin-orbit coupling of p-2CzBN.
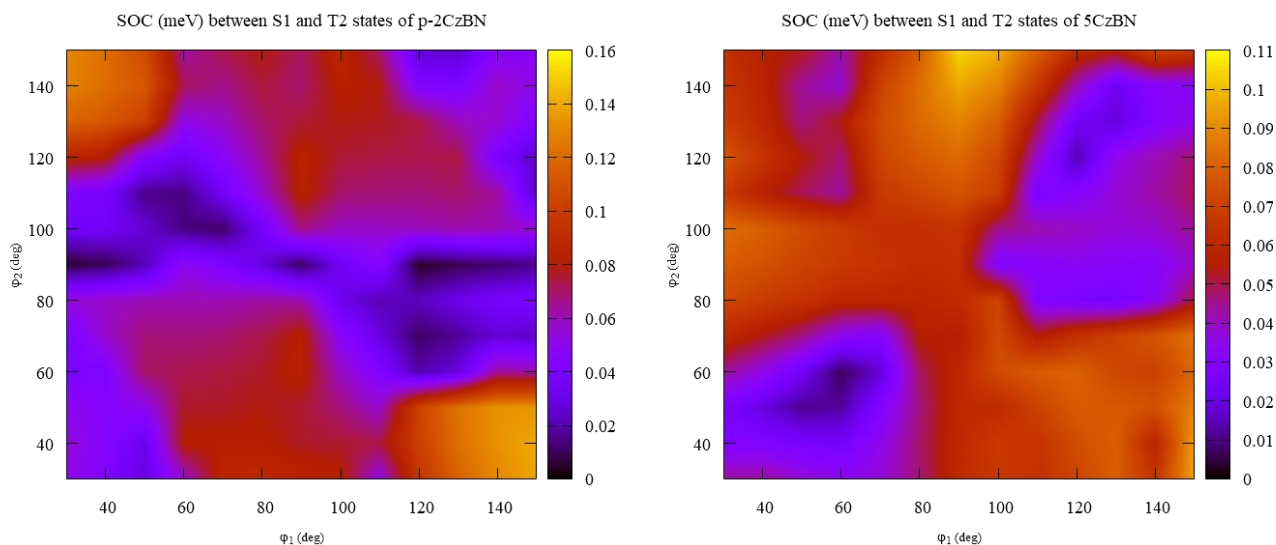
Figure 4.8 Spin-orbit coupling constant (meV) map between S_1 and T_2 state of p-2CzBN (left) and 5CzBN (right) with TDA-PBE1PBE/6-31G**.

In order to calculate the rate of RISC and ISC with Marcus equation (see Chapter 2 for details),

$$k_{RISC} = \frac{2\pi}{\hbar} V_{SOC}^2 \frac{1}{\sqrt{4\pi\lambda kT}} \exp\left[-\frac{(\lambda + \Delta E_{ST})^2}{4\lambda kT}\right]$$

we need to calculate the reorganization energy (λ) for every transition, as schematized in figure 4.9. The reorganization energy of B state with respect to A can be calculated as E(B) with geometry of A subtracted with the E(B) with geometry of B state.

Figure 4.9 Reorganization energy in the final state B upon vertical transition from the initial state A, Q is a generic reaction coordinate representing the geometry differences between states A and B.
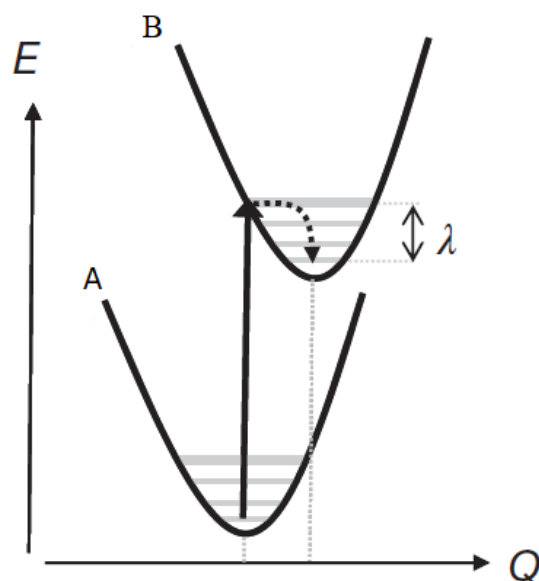
The calculated physical parameters are given in table 4.2. We noted that 5CzBN has a RISC rate, which is the key for TADF performance, higher than p-2CzBN. In p-2CzBN the reverse intersystem crossing process from T_2 to S_1 state has higher rate of RISC than from T_1 to S_1 state. We also note that the small value of the reorganization energy in 5CzBN is the main parameter increasing the rate of RISC with respect to p-2CzBN. The sum of T_1 and T_2 RISC rate of 5CzBN and p-2CzBN are 7.19×10^4 s^{-1} and 2.08×10^4 s^{-1}, respectively. The result shows that the total rate is high enough to drive the TADF process in 5CzBN. But the total rate is high enough to drive the TADF process also in p-2CzBN, if T_2 can be involved: this may not be the case given that it is quite high in energy with respect to T_1. TADF time in 5CzBN shows that it is 4.80×10^{-5} s, while the TADF time of p-2CzBN is 1.39×10^{-5} s which is faster. But when compared (table 4.3) with the TADF time of 2CzBN (inactive molecule previously studied in a similar work) or when compared with the TADF time of 4CzBN (active TADF molecule previous studied in a similar work), p-2CzBN could be a decent TADF emitter.

Table 4.2 Energy gap between singlet and triplet state (ΔE^{ST}), reorganization energy (λ), spin-orbit coupling (V_{SOC}), rate of Reverse InterSystem Crossing (k_{RISC}) and of InterSystem Crossing (k_{ISC}) (at equilibrium geometry). All results are obtained from DFT and TDA calculation performed with the PBE1PBE functional and 6-31G** basis set.

	Transition	ΔE^{ST} (eV)	λ (meV)	V_{SOC} (meV)	Rate	
					k_{RISC} (s^{-1})	k_{ISC} (s^{-1})
p-2CzBN	$S_1 \rightarrow T_1$	-0.290	180.9	0.041	-	3.45×10^7
	$T_1 \rightarrow S_1$	0.290	268.3	0.041	2.49×10^2	-
	$S_1 \rightarrow T_2$	0.110	381.6	0.076	-	1.97×10^5
	$T_2 \rightarrow S_1$	-0.110	268.3	0.076	7.17×10^4	-
	Total rate				7.19×10^4	3.47×10^7
	TADF time (s)				1.39×10^{-5}	
5CzBN	$S_1 \rightarrow T_1$	-0.220	80.5	0.115	-	6.28×10^7
	$T_1 \rightarrow S_1$	0.220	113.3	0.115	2.07×10^4	-
	$S_1 \rightarrow T_2$	-0.170	286.4	0.003	-	1.79×10^5
	$T_2 \rightarrow S_1$	0.170	290.8	0.003	1.26×10^2	-
	Total rate				2.08×10^4	6.30×10^7
	TADF time (s)				4.80×10^{-5}	

Table 4.3 Comparison between the TADF time (s) values of p-2CzBN, 5CzBN, 2CzBN and 4CzBN. The results of p-2CzBN and 5CzBN are obtained from DFT and TDA calculation performed with the PBE1PBE functional and 6-31G** basis set, while the results of 2CzBN and 4CzBN are obtained from DFT and TD-DFT calculation performed with the PBE0 functional and 6-31G* basis set.

	TADF time (s)	TADF active/inactive
p-2CzBN	1.39×10^{-5}	
2CzBN	7.69×10^{-4}	Inactive
4CzBN	2.36×10^{-5}	Active
5CzBN	4.80×10^{-5}	Active

Chapter 5

Conclusions and future outlook

In this work we have theoretically studied, by means of density functional theory (DFT) and TDA-DFT calculations of carbazole benzonitrile derivatives, and addressed the question of how a flexible donor-acceptor (D-A) or a linear donor-acceptor-donor (D-A-D) molecular architecture affects thermally activated delayed fluorescence (TADF) through the nature of excited states, the oscillator strength and the reverse intersystem crossing rates (RISC), also as a function of the conformation of the carbazole side groups and considering the S_0, S_1, T_1 and T_2 electronic states. We focused in particular on two prototypical molecules, p-2CzBN and 5CzBN, that possess a different energy gap between singlet and triplet (ΔE^{ST}). The calculated values of vertical ΔE^{ST} of p-2CzBN and 5CzBN in gas phase (or including an implicit solvation model for toluene) are 0.30 eV and 0.22 eV (0.29 eV and 0.21 eV). p-2CzBN and 5CzBN then could have in principle similar TADF performances, but experimental proofs exist only for the latter compound. We confirmed that the absorption spectrum of 5CzBN is red-shifted, compared to that of p-2CzBN, owing to a more extended delocalization of the frontier orbitals on the carbazole moieties. The torsional energy scans for the rotation of a carbazole group about the carbazole-benzonitrile bond give different profiles for compounds in ground state. The torsional energy maps considering the simultaneous rotation of two flanked carbazoles show that the energy minima in the ground state are located at $\pm 60^{\circ}$, $\pm 50^{\circ}$ and $\pm 120^{\circ}$, $\pm 130^{\circ}$ for p-2CzBN, and at $\pm 60^{\circ}$, $\pm 60^{\circ}$ and $\pm 120^{\circ}$, $\pm 120^{\circ}$ for 5CzBN, while the barrier for interconverting between the minima is located at $\pm 90^{\circ}$ for both molecules (when carbazole planes are perpendicular to the benzonitrile ring). Also, for p-2CzBN the T_1 state profile shares the same minima as the ground state, while in S_1 state the absolute minimum is found at $\pm 90^{\circ}$.

We also investigated the oscillator strength and the nature of excited states, either being of charge transfer (CT) or locally excited (LE) character. The slightly higher oscillator strength of p-2CzBN with respect to 5CzBN is one of the factors that leads us to think that p-2CzBN is also a TADF active emitter. Both 5CzBN and p-2CzBN exhibit a CT character in both S_1 and S_2 states, while T_1 exhibits a LE character. Interestingly, T_2 in 5CzBN shows a CT character, while in p-2CzBN shows a mixed character in between CT and LE. We also found that, unlike, p-2CzBN, the energy of T_2 in 5CzBN is below that of S_1 state, a strong argument supporting the involvement of this further state, besides T_1, in the TADF process.

The spin-orbit couplings (V_{SOC}) and reorganization energies (λ) were calculated in order to determine the rate of (Reverse) InterSystem crossing, which is the rate determining-step for light emitting in TADF based-OLEDs. The rate of RISC of p-2CzBN from T_2 to S_1 is surprisingly high compared to T_1 to S_1 and to the same process in 5CzBN, since from EL-Sayed rules, this transition should be less favored for p-2CzBN being T_2 (CT/LE) more similar to S_1 (CT). The sum of T_1 and T_2 RISC rates (k_{RISC} is 7.19×10^4 s^{-1} and TADF time is 1.39×10^{-5} s) is low enough to drive the TADF process in p-2CzBN, while the total RISC rate in 5CzBN (k_{RISC} is 2.08×10^4 s^{-1} and TADF time is 4.80×10^{-5} s) is lower. The lower reorganization energies in 5CzBN seem to be the dominant factor in determining the higher RISC rate between T_1 and S_1. The summary of TADF mechanism and all the calculated values in gas phase are schematized in figure 5.1 and 5.2.
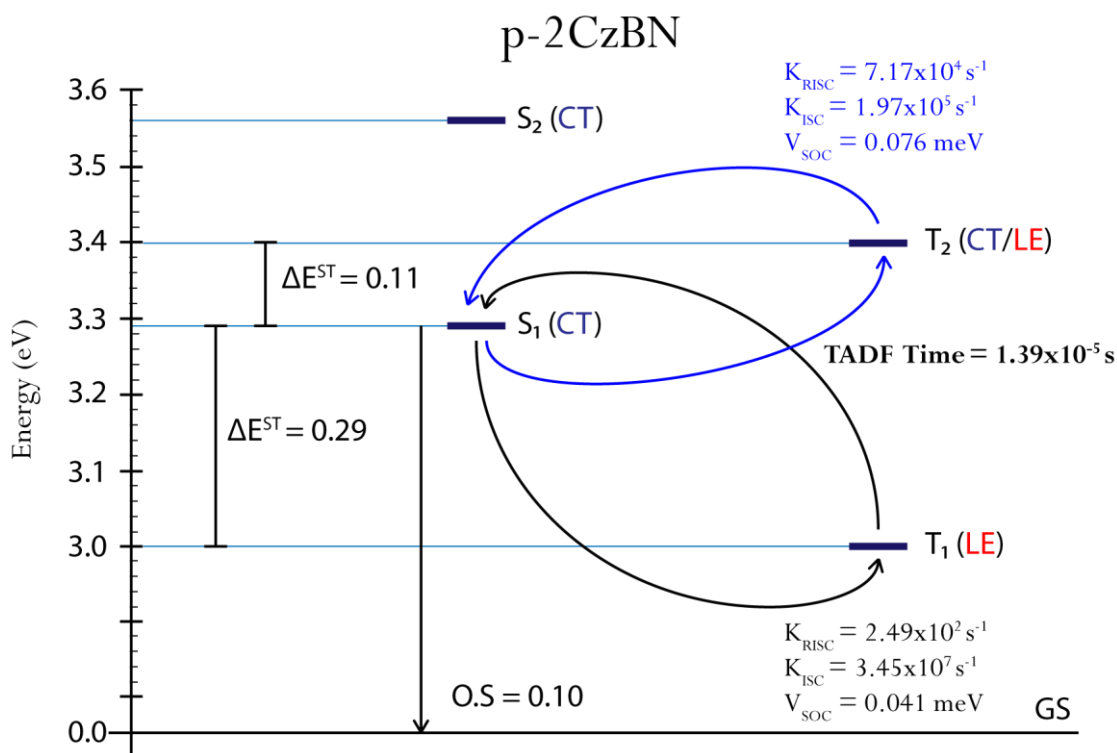

Figure 5.1 The proposed scheme of TADF mechanism in p-2CzBN. All the results were obtained by means of DFT and TDA-DFT calculations with the PBE1PBE/6-31G**.
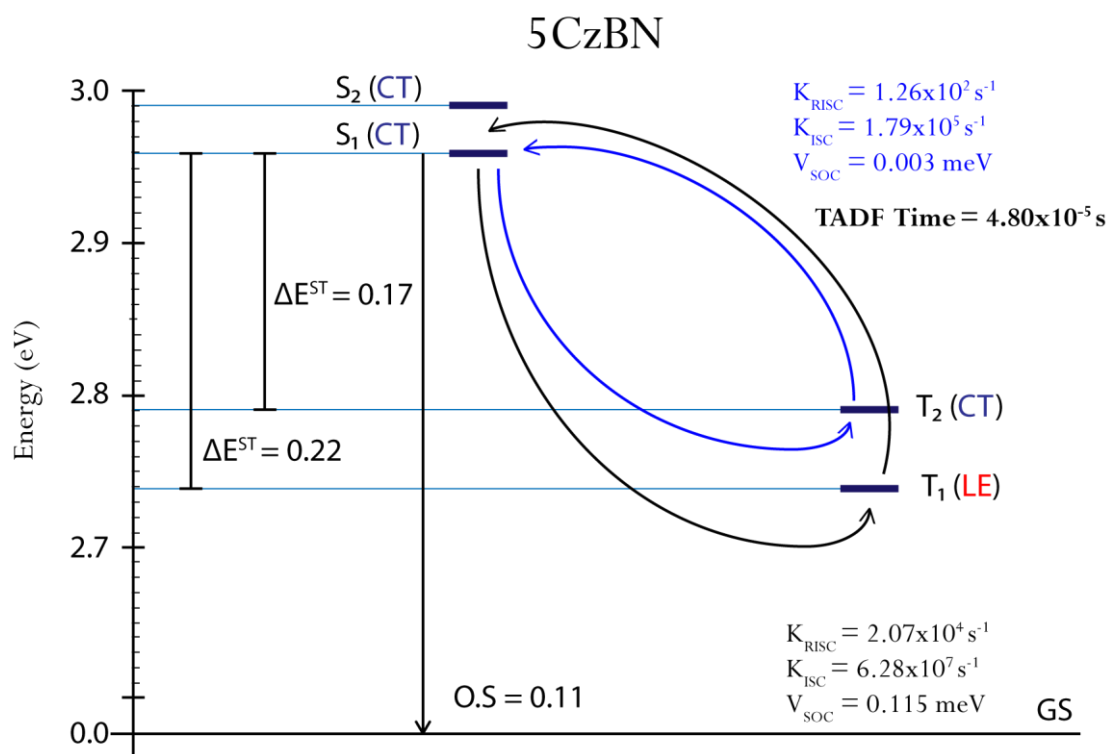
Figure 5.2 The proposed scheme of TADF mechanism in 5CzBN. All the results were obtained by means of DFT and TDA-DFT calculations at PBE1PBE/6-31G** level.

As for outlooks, we noticed that in calculations carried out with an implicit solvation model for toluene (the solvent employed in the experiments), the oscillator strength is a bit higher than in gas phase, and also reorganization energies are expected to change. Therefore, taking into account solvent effects could improve the accuracy of the calculation predictions and will be the subject of future investigation.

Bibliography

1. www.businesskorea.co.kr/news/articleView.html?idxno=19411, www.pulsenews.co.kr/view.php?year=2017&no=852666, www.iphoneitalia.com/580413/nel-2018-arrivera-il-primo-iphone-con-display-curvo.

2. Tang, C. W. & Van Slyke, S. A. Organic electroluminescent diodes. *Appl. Phys. Lett.* **51**, 913–915 (1987).

3. Chen, H.-W., Lee, J.-H., Lin, B.-Y., Chen, S. & Wu, S.-T. Liquid crystal display and organic light-emitting diode display: present status and future perspectives. *Light Sci. Appl.* **7**, 17168 (2018).

4. Nakanotani, H. *et al.* High-efficiency organic light-emitting diodes with fluorescent emitters. *Nat. Commun.* **5**, 1–7 (2014).

5. Lin, L. *et al.* Photo- and electro-luminescence of three TADF binuclear Cu(i) complexes with functional tetraimine ligands. *J. Mater. Chem. C* **5**, 4495–4504 (2017).

6. Minaev, B., Baryshnikov, G. & Agren, H. Principles of phosphorescent organic light emitting devices. *Phys. Chem. Chem. Phys.* **16**, 1719–1758 (2014).

7. Udagawa, K., Sasabe, H., Cai, C. & Kido, J. Low-driving-voltage blue phosphorescent organic light-emitting devices with external quantum efficiency of 30%. *Adv. Mater.* **26**, 5062–5066 (2014).

8. Chihaya, A. Third-generation organic electroluminescence materials. *Jpn. J. Appl. Phys.* **53**, 60101 (2014).

9. Delorme, R. & Perrin, F. Durées de fluorescence des sels d'uranyle solides et de leurs solutions,. *J. Phys. le Radium* **10**, 177–186 (1929).

10. Tao, Y. *et al.* Thermally activated delayed fluorescence materials towards the breakthrough of organoelectronics. *Adv. Mater.* **26**, 7931–7958 (2014).

11. Olivier, Y., Moral, M., Muccioli, L. & Sancho-García, J. C. Dynamic nature of excited states of donor-acceptor TADF materials for OLEDs: How theory can reveal structure-property relationships. *J. Mater. Chem. C* **5**, 5718–5729 (2017).

12. Im, Y. *et al.* Molecular Design Strategy of Organic Thermally Activated Delayed Fluorescence Emitters. *Chem. Mater.* **29**, 1946–1963 (2017).

13. Dias, F. B., Penfold, T. J., Berberan-Santos, M. N. & Monkman, A. P. Photophysics of Thermally Activated Delayed Fluorescence in Organic Molecules. 227–261 (2018).

14. Hosokai, T. *et al.* Solvent-dependent investigation of carbazole benzonitrile derivatives: does the LE3−CT1 energy gap facilitate thermally activated delayed fluorescence? *J. Photonics Energy* **8**, 1 (2018).

15. Chen, T. *et al.* Understanding the Control of Singlet-Triplet Splitting for Organic Exciton Manipulating: A Combined Theoretical and Experimental Approach. *Sci. Rep.* **5**, 1–11 (2015).

16. Dias, F. B. *et al.* The role of local triplet excited states and D-A relative orientation in thermally activated delayed fluorescence: Photophysics and devices. *Adv. Sci.* **3**, 1–10 (2016).

17. Nobuyasu, R. S. *et al.* The influence of molecular geometry on the efficiency of thermally activated delayed fluorescence. *J. Mater. Chem. C* **7**, 6672–6684 (2019).

18. Hosokai, T. *et al.* Evidence and mechanism of efficient thermally activated delayed fluorescence promoted by Delocalized Excited States. Sci. Adv. 3, e1603282 (2017)

19. Anna, K. & Heinz, B., Electronic processes in organic semiconductors: An introduction. Wiley (2015).

20. Li, S. W. *et al.* Cyanopyrimidine-Carbazole Hybrid Host Materials for High-Efficiency and Low-Efficiency Roll-Off TADF OLEDs. *ACS Appl. Mater. Interfaces* **10**, 12930–12936 (2018).

21. Wex, B. & Kaafarani, B. R. Perspective on carbazole-based organic compounds as emitters and hosts in TADF applications. *J. Mater. Chem. C* **5**, 8622–8653 (2017).

22. Valeur, B. *Molecular Fluorescence: Principles and Applications* **8**, (2001).

23. Bañares, L. Unexpected intersystem crossing. *Nat. Chem.* **11**, 103–104 (2019).

24. Shakeel, U. & Singh, J. Study of processes of reverse intersystem crossing (RISC) and thermally activated delayed fluorescence (TADF) in organic light emitting diodes (OLEDs). *Org. Electron. physics, Mater. Appl.* **59**, 121–124 (2018).

25. Marian, C. M. Spin-orbit coupling and intersystem crossing in molecules. *Wiley Interdiscip. Rev. Comput. Mol. Sci.* **2**, 187–203 (2012).

26. Olivier, Y. *et al.* Nature of the singlet and triplet excitations mediating thermally activated delayed fluorescence. *Phys. Rev. Mater.* **1**, 1–6 (2017).

27. Uoyama, H., Goushi, K., Shizu, K., Nomura, H. & Adachi, C. Highly efficient organic light-emitting diodes from delayed fluorescence. *Nature* **492**, 234–238 (2012).

28. Turro, N. J., Ramamurthy, V. & Scaiano, J. C. Modern Molecular Photochemistry of Organic Molecules. *Photochem. Photobiol.* **88**, 1033–1033 (2012).

29. Foresman, J. & Frisch, Æ. Exploring Chemistry With Electronic Structure Methods.pdf. *Exploring Chemistry with Electronic Structure Methods* 302 (1996).

30. Moral, M., Muccioli, L., Son, W. J., Olivier, Y. & Sancho-Garcia, J. C. Theoretical rationalization of the singlet-triplet gap in oleds materials: Impact of charge-transfer character. *J. Chem. Theory Comput.* **11**, 168–177 (2015).

31. Etienne, T., Assfeld, X. & Monari, A. Toward a quantitative assessment of electronic transitions" charge-transfer character. *J. Chem. Theory Comput.* **10**, 3896–3905 (2014).

32. Etienne, T., Assfeld, X. & Monari, A. New insight into the topology of excited states through detachment/attachment density matrices-based centroids of charge. *J. Chem. Theory Comput.* **10**, 3906–3914 (2014).

33. Guido, C. A., Cortona, P., Mennucci, B. & Adamo, C. On the metric of charge transfer molecular excitations: A simple chemical descriptor. *J. Chem. Theory Comput.* **9**, 3118–3126 (2013).